RESEARCH

Surrogate models in convection-dominated fault systems: considerations for efficient and reliable realizations

Thomas Simader[1,2,3] · Denise Degen[4,5] · Tobias Meier[1] · Horst Rüter[3] · Florian Wellmann[2,6]

Received: 25 November 2025 / Accepted: 18 April 2026

Abstract
Efficiently solving partial differential equations in geothermal systems is increasingly important, particularly for coupled processes. Accurately describing these systems usually involves high-dimensional parameter spaces and computationally expensive forward simulations, which makes the exploration of multiple scenarios for uncertainty quantification or sensitivity analysis challenging. Surrogate modeling helps overcome this barrier by significantly reducing the computation time. However, the partial differential equations can exhibit non-linear and chaotic behavior when natural convection occurs, which might complicate surrogate modeling. In geothermal systems, where fault zones act as preferential fluid pathways leading to convection, geological conditions and physical properties sometimes allow multiple numerical solutions for the same external conditions. Slight variations in parameters or numerical schemes can produce distinct convection regimes, resulting in both physical and numerical challenges. In this study, we construct surrogate models of an idealized thermo-hydraulic fault model using the non-intrusive reduced basis method, which integrates physics-based and data-driven approaches. By incorporating physical preconditioning, exploring possible bifurcation points, and using entropy generation-based surrogates, we demonstrate enhanced surrogate model accuracy. This work highlights key considerations for constructing effective surrogate models in convection-dominated systems.

Keywords Natural convection · Surrogate modeling · Entropy · Faults · Machine learning · Geothermal

1 Introduction

The need to accelerate the numerical solution of systems governed by partial differential equations (PDEs) is increasingly essential. Whereas purely conductive thermal models once described geothermal studies, it is now state of the art to consider coupled thermo-hydraulic-mechanical (THM) systems, and sometimes also chemical processes and phase-changes [1–5]. These coupled systems lead to more complex PDEs, which may be non-linear and chaotic, such as in convective systems [6]. Therefore, in systems affected by natural convection, temperature predictions at depth become progressively more uncertain [7]. Convective systems also involve high-dimensional parameter spaces and numerous degrees of freedom, leading to computationally expensive forward simulations. Unfortunately, understanding the underlying physical processes - and thereby enabling informed decision-making - requires extensive parameter studies, sensitivity analyses, and uncertainty quantification [4, 8]. Additionally, in forecasting and monitoring applications, it is often desirable to establish a digital twin of the system with an efficient forward computation [9]. Surrogate models have proven to be a powerful tool to enable such studies.

https://doi.org/10.1007/s10596-026-10421-w

Published online: 21 May 2026

 https://doi.org/10.1007/s10596-026-10421-w

Although various types of surrogate models have been successfully created for different geothermal applications [10–12], their use in dynamical systems, such as convective systems, remains challenging due to both physical and numerical complexities. Such systems can involve fault zones that act as a preferential pathway and generate thermal anomalies through density-driven hydrothermal convection. Fault zones can exhibit significant geothermal potential and might play an essential role in the success of deep geothermal systems [13–16]. Recent studies even indicate that the potential of high-temperature geothermal systems around crustal fault zones is underestimated [17, 18].

From a geological perspective, characterizing the temperature regime at fault zones is associated with high uncertainties in their petrophysical, hydraulic, and structural properties [19]. Even over short distances, faults show significant variation in complexity along strike and dip [20]. The physical complexity arises from the fact that in these systems, even under fixed external conditions, the equations of motion can allow multiple stable solutions. Another characteristic is the potential for chaotic states, where irregular behavior can persist indefinitely, even when external conditions remain constant, and the high sensitivity of the solution to initial conditions [21, 22]. Also, the morphology and magnitude of convection cells are sensitive to the permeability distribution and orientation of the fault zone [23, 24]. The numerical complexity arises because different models with slightly different parameters, numerical solvers, or spatial and temporal discretizations can arbitrarily result in one of the possible stable solutions [25, 26]. However, numerical stability requires the same solution to be obtained for the same input. To the best of our knowledge, no surrogate model for a system that includes convection at a fault has been created to date.

In this paper, we investigate various approaches to efficiently generate a surrogate model of the thermal state at a fault and examine the associated numerical and physical challenges. We use the non-intrusive reduced basis (NI-RB) method, a physics-based machine learning method which combines physics-based and data-driven approaches [27, 28]. In the context of geoscientific applications, it has proven to provide speed-ups of three to six orders of magnitude depending on the problem and the number of time steps [4]. Beyond conventional metrics from the machine learning community, we use the entropy generation number N_s to characterize the behavior of the non-linear geothermal system [29, 30]. We propose that physical preconditioning, analyzing possible bifurcation points, and using entropy generation-based surrogates can significantly enhance the performance of the surrogate model.

2 Background and methods

In the following, we present the governing equations for thermo-hydraulic (TH) modeling. Afterward, we introduce the parameters controlling the convective behavior, the concept of entropy generation, and the NI-RB method, which is responsible for constructing the surrogate models.

2.1 Governing equations

The numerical solution of TH coupled PDEs is performed with the finite-element software package COMSOL Multiphysics® (Version $\geq$ 6.2). The continuity equation for a 3D porous medium, including Darcy's law, is [31, Eq. 4.16]:

$$\begin{aligned} \frac{\partial}{\partial t}(\varphi\rho_f) + \nabla\cdot(\rho_f \vec{v}_D) &= q_f, \\ \vec{v}_D &= -\frac{\vec{k}}{\mu_f}(\nabla p - \rho_f \vec{g}), \end{aligned} \tag{1}$$

where φ is the porosity, ρ the density, q the fluid source term, $\vec{v}_D$ the Darcy velocity, $\vec{k}$ the permeability (in this study isotropic), μ the dynamic viscosity, $\vec{g}$ the gravitational acceleration, and p the pressure. The subscript f denotes fluid properties. This PDE is known as the groundwater flow equation in its pressure formulation, since pressure p is the sole primary variable. The fluid density and viscosity are expressed as functions of p and temperature T, following the formulation of Zyvoloski et al. [32].

Following the discrete fracture matrix (DFM) approach, faults are represented explicitly as lower-dimensional geometric objects (2D surface) embedded in a porous matrix [33]. This approach is common for modeling geothermal systems where faults or fractures have a strong structural influence on flow and transport processes [5, 13, 34, 35]. The continuity equation is solved for the in-plane components (tangential to the fault plane) [36, Eq. 4.24]:

$$\begin{aligned} d_F \frac{\partial}{\partial t}(\varphi_F \rho_f) + \nabla_T \cdot (d_F \rho_f \vec{v}_{D,T}) &= d_F q_f, \\ \vec{v}_{D,T} &= -\frac{\vec{k}_{F,T}}{\mu_f}(\nabla_T p - \rho_f \vec{g}_T), \end{aligned} \tag{2}$$

where d is the thickness and the subscripts T and F denote the tangential component and fault properties, respectively. In Eq. 2, the fault is considered a porous medium where the lower-dimensional element is transversally "invisible". While this makes the model effective for longitudinal flow in permeable faults, it is incapable of representing them as low-permeability barriers [35]. Consequently, this study assumes that faults act as a hydraulic conduit embedded in a low permeable matrix.

Considering a local thermal equilibrium and no internal heat source, the heat equation in the 3D medium is solved for [37, Eq. 2.3]:

$$\rho_m c_{p,m} \frac{\partial T}{\partial t} + \rho_f c_{p,f} \vec{v}_d \cdot \nabla T = \lambda_m \nabla^2 T + q_0, \tag{3}$$

where c_p represents the isobaric heat capacity and λ is the thermal conductivity. The subscript m refers to bulk medium properties, calculated as the weighted arithmetic mean of the solid (s) and fluid (f) phases:

$$\rho_m c_{p,m} = (1 - \varphi)\rho_s c_{p,s} + \varphi \rho_f c_{p,f} \tag{4}$$

$$\lambda_m = (1 - \varphi)\lambda_s + \varphi \lambda_f \tag{5}$$

At the fault, Eq. 3 becomes [38, Eq. 4.85]:

$$d_F \rho_{m,F} c_{p,m,F} \frac{\partial T}{\partial t} + d_F \rho_f c_{p,f} \vec{v}_{D,T} \cdot \nabla_T T = d_F \lambda_{m,F} \nabla_T^2 T + q_0, \tag{6}$$

where the additional source term q_0 represents the out-of-plane heat flux transferred from the domain to the fault.

2.2 Convection

The scenario considered in this study can be regarded as an extension of the Horton-Rogers-Lapwood problem [39, 40], the porous media analogue of the Rayleigh-Bénard problem, to a 3D fault system (Fig. 1). In its original formulation, a homogeneous porous medium with finite vertical thickness and infinite horizontal extent is placed between perfect heat conductors. The fluid is driven by a temperature difference ΔT imposed between the plates. Due to thermal expansion, the fluid at the bottom is less dense, establishing an inherently unstable state under gravity [21]. As the fluid cannot rise as a whole since it is a closed system, instability occurs once the imposed temperature difference is sufficient to overcome the stabilizing effects of thermal conduction and viscosity. The Darcy-modified Rayleigh number Ra characterizes the onset of convection and is a dimensionless control parameter that measures the ratio of the destabilizing buoyancy force to the stabilizing dissipative forces [6, Eq. 12.89]:

$$\mathrm{Ra} = \frac{g\,\alpha_f\,\rho_f^2\,c_{p,f}\,k\,H\,\Delta T}{\mu_f\,\lambda_m}. \tag{7}$$

Here, α_f is the thermal expansion coefficient of the fluid and H is the height of the system. If Ra is below the critical value $\mathrm{Ra_c}$, there is only one uniform "conducting" solution to the system in the form of a constant temperature gradient $T(x, y, z) = T_0 + z \cdot (\Delta T/H)$ [37, Eq. 6.8]. If $\mathrm{Ra} \geq \mathrm{Ra_c}$, natural convection will take place in the porous medium. The non-trivial solution to $\mathrm{Ra_c}$ is called the fundamental convective flow of the system [41]. As Ra increases, the flow turns time-dependent, undergoing a series of bifurcations that progress from periodic to quasiperiodic and eventually to chaotic behavior [42]. Depending on the initial condition (IC), multiple solutions can coexist within certain parameter ranges in convection problems [43].

Two dimensionless parameters further control the flow dynamics. First, the Prandtl number Pr, defined as the ratio of thermal to viscous damping mechanisms acting on the fluid [37, Eq. 6.19],

$$\mathrm{Pr} = \frac{\mu_f c_{p,f}}{\lambda_m}, \tag{8}$$

controls the domain sizes of equilibrium state and dynamic solutions [21].

In general, natural convection tends to reach an equilibrium state when Pr is high and Ra is low, while more complex and unstable flow patterns typically occur at low Pr and high Ra [44]. The second parameter controlling the solution is the aspect ratio of lateral to vertical extent h. Beck [45] successfully determined the preferred cellular modes of convection patterns at the onset of convection for different aspect ratios in a 3D medium.

An equilibrium solution can be forced using suitable IC by a guess based on a Fourier series that matched the boundary conditions (BCs) [46, Eq. 12]:

$$T(x, y, z) = A \sin\left(\frac{\pi z}{H}\right) \cos\left(\frac{m\pi x}{H h_x}\right) \cos\left(\frac{n\pi y}{H h_y}\right) + 1 - \frac{z}{H}. \tag{9}$$

$\mathrm{Ra_c}$ is strongly influenced by the specific problem setup and has been the subject of extensive investigations. In the Horton-Rogers-Lapwood problem, the critical Rayleigh number is equal to $4\pi^2$ [40]. Nield [47] demonstrated that $\mathrm{Ra_c}$ can range from three to $4\pi^2$ for the same problem setup, depending on the prescribed BCs. Moreover, Ra_c further decreases when considering a temperature-dependent fluid viscosity instead of a temperature-independent one [48]. When it comes to faults, analytical expressions have been developed: Murphy [49] and Zhao et al. [41] assume a temperature-independent viscosity in their calculations. However, viscosity is known to significantly affect the onset of convection [48], which may limit the applicability of their expressions to real-world scenarios. In contrast, the formulation from Malkovsky and Magri [50] accounts for a temperature-dependent viscosity.

Nevertheless, Ra has limited applicability in geothermal applications because its constituent parameters (Eq. 7) are rarely constant in real-world systems. Geological systems often involve heterogeneous, anisotropic media and complex geometries for which no analytical expressions for Ra exist. Then, these parameters are typically simplified through domain-averaging, which can yield similar Ra values for systems that behave differently in reality. For example, Niederau et al. [30] found that varied permeability distributions with the same harmonic average produced different outcomes, with convection occurring in some regions while others remained conductive. Thus, a representative Ra that universally characterizes convection in heterogeneous or layered porous media does not exist [51].

2.3 Entropy generation

While Ra provides a predictive measure of the system behavior, the assessment of the entropy generation has proven to be a valuable diagnostic tool [30]. Convective heat transfer through fluid-saturated porous media is inherently irreversible, arising from two main sources: (1) transfer of heat in the direction of finite temperature gradients and (2) fluid friction from viscous flow through the pores [6]. For a general three-dimensional convection process, the local rate of volumetric entropy generation S'''_{gen} is [6, Eq. 12.39]:

$$S'''_{\text{gen}} = S'''_{\text{therm}} + S'''_{\text{visc}} = \underbrace{\frac{\lambda}{T_0^2}(\nabla T)^2}_{\geq 0} + \underbrace{\frac{\mu_f}{kT_0}(\vec{v}_D)^2}_{\geq 0} \geq 0, \tag{10}$$

where the first term accounts for heat transfer and the second term for fluid friction. The entropy generation number N_s is the dimensionless form of Eq. 10 over the volume and by definition the ratio of the actual entropy generation rate S'''_{gen} to the minimum (characteristic) entropy transfer rate S'''_{min} [52, 53]:

$$S'''_{\text{min}} = \left[\frac{q^2}{\lambda T_0^2}\right] = \left[\frac{\lambda(\Delta T)^2}{H^2 T_0^2}\right], \tag{11}$$

$$N_s = \frac{\int_V S'''_{\text{gen}}\, dV}{\int_V S'''_{\text{min}}\, dV}. \tag{12}$$

The first term in square brackets in Eq. 11 corresponds to isoflux BCs, while the second term applies to isothermal ones [54].

Börsing et al. [29] analyzed the transient behavior of entropy generation for systems with different geothermal gradients. A value of $N_s \approx 1$ suggests a conduction-dominated system, whereas higher values indicate a convection-dominated one. In a convective system at an equilibrium state, entropy generation increases to a peak before relaxing into a steady-state plateau, corresponding to the state where a quasi-static thermodynamic equilibrium is reached. This finding is consistent with the study of Magherbi et al. [55], who found that fluctuations in total entropy generation indicate oscillatory flow influenced by BCs when natural convection occurs. Moreover, the entropy generation at dynamic equilibrium is proportional to the initial temperature gradient, which further indicates the suitability of using entropy generation as a measure of hydrothermal state.

The Bejan number Be is defined as $S'''_{\text{therm}}/S'''_{\text{gen}}$ [52]. Be $= 1$ represents the limit where heat transfer irreversibility is dominant, while Be $= 0$ represents irreversibility entirely due to fluid friction. The case of Be $= 0.5$ corresponds to a condition where the entropy generation rates from heat transfer and fluid friction are equal. Börsing et al. [29] and Niederau et al. [7] found that in geothermal systems Be ≈ 1, indicating that viscous dissipation effects are negligible. Therefore, we assume in the following that $S'''_{\text{gen}} = S'''_{\text{therm}}$.

2.4 Non-intrusive reduced basis method

The NI-RB method is a projection-based model order reduction technique that reduces degrees of freedom while preserving the input-output relationship. It consists of two phases: the offline and online stages. During the offline stage, the surrogate model is constructed, including all computationally expensive tasks. After its construction, the surrogate can be used in the online stage for fast and efficient forward evaluations [27, 56]. The reduced solution u_{rb} is a linear combination of the reduced coefficients $\theta^{(i)}_{\text{rb}}$ and the basis functions ψ_i that span the reduced space V_{rb}:

$$u_{\text{rb}}(\vec{\mu}) = \sum_{i=1}^{r} \theta^{(i)}_{\text{rb}}(\vec{\mu})\psi_i \qquad \in V_{\text{rb}}, \tag{13}$$

https://doi.org/10.1007/s10596-026-10421-w

where $\vec{\mu}$ are the model parameters. Before constructing the surrogate model, it is necessary to generate n_t training snapshots of full-order solutions through forward simulations. In this study, we use between 100 and 200 training snapshots depending on the number of parameters. The parameters are sampled with the quasi-random Latin Hypercube sampling strategy [57]. Next, basis functions are selected using r modes of the Proper Orthogonal Decomposition (POD) from the training snapshots. This involves performing a singular value decomposition and truncating the resulting singular vectors based on a user-defined threshold ϵ. The cumulative energy criterion assesses the singular values σ to choose r modes from the basis functions, where the basis functions correspond to the most influential singular vectors [28, 56, Eq. 3]:

$$\frac{\sum_{i=1}^{r} \sigma_i^2}{\sum_{i=1}^{n_t} \sigma_i^2} \leq \epsilon. \tag{14}$$

In the next step of the offline stage, the coefficients $\theta_{\text{rb}}^{(i)}$ depending on the parameters $\vec{\mu}$ are determined, which can be considered as a regression problem. As the governing equations are non-linear, we use feed-forward neural networks for this step, implemented with the Pytorch [58] and Lightning [59] Python libraries. During training, the parameters serve as features, and the matrix product of the basis functions and the training snapshots as data. Before constructing the surrogate model, it is important to scale both the snapshots and the parameters. The respective scaling norms will be indicated for every surrogate model presented in this manuscript. We perform hyperparameter optimization using the Optuna Python package [60]. Once a model mapping $\vec{\mu}$ onto $\theta_{\text{rb}}^{(i)}$ is found, the online stage can be performed according to Eq. 13. More details about the implementation of NI-RB can be found in Hesthaven and Ubbiali [27] and Degen et al. [56].

The predictive accuracy of the surrogate models is assessed using the mean squared error (MSE) between each node of the full-order model and surrogate model, defined as follows:

$$\text{MSE} = \frac{1}{N} \sum_{j=1}^{N} (u_{\text{true},j} - u_{\text{rb},j})^2. \tag{15}$$

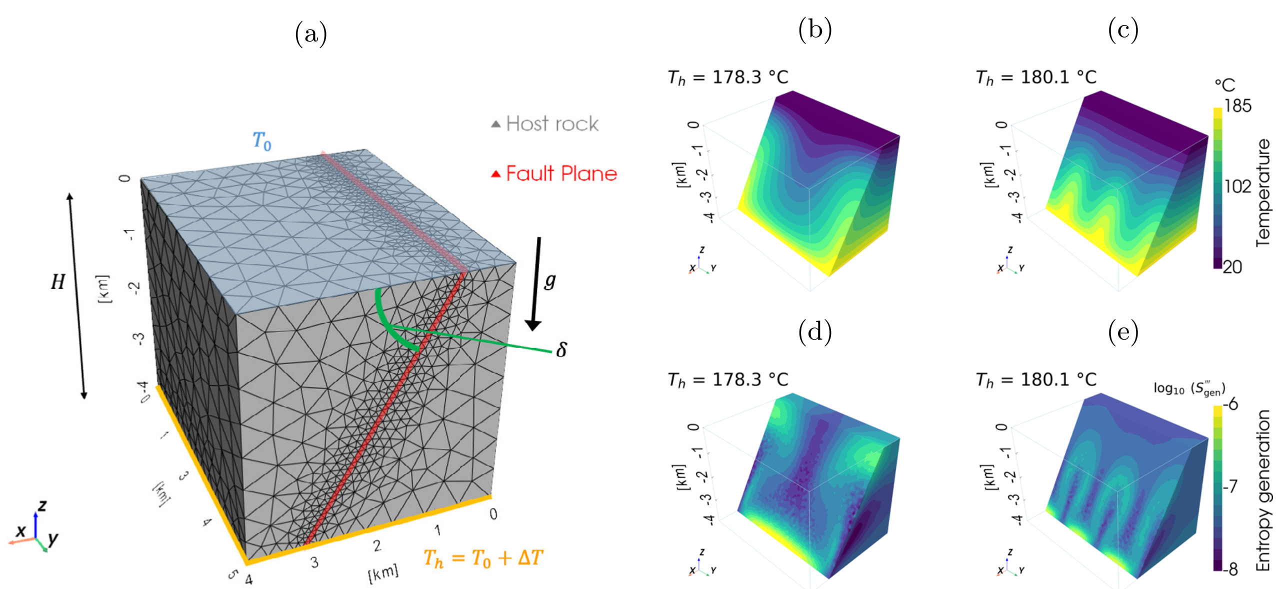

Fig. 1 (**a**) Schematic representation of the synthetic model. (**b**) and (**c**) show the temperature distribution for two distinct values of T_h with all other parameters fixed as indicated in Table 1, which results in two and five stable convection cells at 1×10^{13} s simulation time. (**d**) and (**e**) show the corresponding entropy generation

Also, we evaluate the MSE and correlation coefficient (R^2) of N_s between the full-order model and surrogate model:

$$\mathrm{MSE}_{Ns} = \frac{1}{N}\sum_{j=1}^{N}(N_{s,\mathrm{true},j} - N_{s,\mathrm{rb},j})^2, \tag{16}$$

$$R^2 = \frac{\sum_{j=1}^{N}(N_{s,\mathrm{rb},j} - \bar{N}_{s,true})^2}{\sum_{j=1}^{N}(N_{s,\mathrm{true},j} - \bar{N}_{s,true})^2}, \tag{17}$$

where $\bar{N}_s$ denotes the average N_s. Lower MSE values and R^2 values closer to 100 % indicate a better predictive performance of the surrogate model. The additional evaluation of N_s provides physical insights into model reliability that standard statistical metrics (MSE) might overlook.

3 Synthetic model

As implied in the previous section, we consider a two-component model to investigate the potential of the NI-RB method to construct reliable surrogate models. The synthetic model (Fig. 1) consists of a host rock and a fault. Its vertical extent is $H = 4$ km, while the horizontal dimensions measure 4 km in the x-direction and 5 km in the y-direction (parallel to the strike of the fault). Thus, the aspect ratios of the domain are $h_y = 1.25$ and $h_x = 1.00$. Dirichlet temperature BCs are prescribed at the top and bottom boundaries, while the vertical boundaries are assumed to be adiabatic. No-flow BCs are applied for the pressure component on all boundaries, while pointwise constraint pressure BCs are imposed at the top four corner points to guarantee a solution. Discretization is carried out using tetrahedral elements, with a maximum resolution of 100 m along the fault and 500 m in the host rock (1a).

With these mesh settings, the model has been validated against the "3D Benchmark of Free Thermal Convection in a Faulted System" from Magri et al. [65]. The benchmark originally modeled the fault as a 3D equivalent porous medium, employing a mesh of rectangular bricks that is specifically refined near the fault. We reproduce the same solution for the temperature and velocity field for the DFM and 3D approach with a tolerance of 0.6 °C and $1.2 \times 10^{-9}\,\mathrm{m\,s^{-1}}$. The comparison is shown in the supplementary material. We justify the use of the DFM approach because it results in significantly fewer degrees of freedom in the finite element model compared to equidimensional representations (2.2×10^5 vs. 8.8×10^5), thereby reducing the computational cost of the simulations by a factor of approximately 13. The resulting faster evaluation of the full-order model was particularly helpful when experimenting with surrogate modeling, as the NI-RB method relies on the generation of a large number of a priori snapshots.

Throughout the study, we will investigate surrogate models with different spans of parameter spaces listed in Table 1. The parameter ranges are extracted from published databases and the literature indicated in the footnotes of the table. Accounting for non-constant fluid properties, Ra values in this study range from 0.02 to 0.7 in the host rock and between 474 and 11535 at the fault, based on the reference values in Table 1.

4 Results

In the following, we present the construction of surrogate models that capture the system's thermal state. To assess the influence of different sources of uncertainty, we first vary parameters individually and eventually analyze their combined effects, adopting a similar approach to Degen et al. [66]. Validation of the NI-RB approach is carried out by comparing surrogate model predictions against full-order solutions obtained from randomly sampled test parameter sets. In addition to standard performance metrics, N_s is evaluated as an indicator of model reliability.

 https://doi.org/10.1007/s10596-026-10421-w

Table 1 Fixed and free parameters of the surrogate models that will be investigated in this study. The parameter ranges are chosen to be consistent with datasets and case studies as specified below the table

Parameter	Symbol	Reference value	Range	Unit
BC				
Top temperature	T_0	20	-	°C
Bottom temperature	$T_h = T_0 + \Delta T$	180	130 to 220[1]	°C
Fault				
Dip	δ	60	55 to 90[2]	°
Thermal Conductivity	λ_F	2	2 to 4[3]	$\mathrm{W\,m^{-1}\,K^{-1}}$
Volumetric heat capacity	$c_{p,F}\ \rho_{s,F}$	2×10^6	-	$\mathrm{J\,K^{-1}\,m^{-3}}$
Porosity	φ_F	20	1 to 25[3]	%
Permeability	k_F	1.5×10^{-13}	10^{-14} to 10^{-12}[2]	$\mathrm{m^2}$
Fault width	d_F	50	-	m
Host rock				
Thermal Conductivity	λ	2	2 to 4[4]	$\mathrm{W\,m^{-1}\,K^{-1}}$
Volumetric heat capacity	$c_p\ \rho_s$	2×10^6	-	$\mathrm{J\,K^{-1}\,m^{-3}}$
Porosity	φ	0.1	0.1 to 15[4]	%
Permeability	k	10^{-17}	10^{-17} to 10^{-15} [2]	$\mathrm{m^2}$
Fluid				
Thermal Conductivity	λ_f	0.65	-	$\mathrm{W\,m^{-1}\,K^{-1}}$
Specific heat capacity	$c_{p,f}$	4200	-	$\mathrm{J\,K^{-1}\,kg^{-1}}$

[1] [17, 61].
[2] [62].
[3] [63].
[4] [64]

4.1 Surrogates for the temperature and entropy generation field (Varying T_h)

For the construction of the first surrogate model, only the bottom temperature T_h is varied in 150 training snapshots. As shown in Eq. 7, it is directly proportional to Ra and thus directly affects the convective behaviour of the system. Plotting T_h against N_s of the training snapshots (Fig. 2) reveals a bifurcation diagram. When $T_h < 143\,°\mathrm{C}$, only conducting solutions exist where N_s is close to one. For $T_h \geq 143\,°\mathrm{C}$, which corresponds to $\mathrm{Ra_c}$ in this model, the first bifurcation happens, resulting in a solution with two convection cells and increasing entropy generation. By definition, a convection cell or cellular mode contains one upwelling and one downwelling region [29]. As T_h increases, up to four different convection regimes can coexist for similar T_h values. In total, two to seven convection cells are observed in Fig. 2. If more training snapshots were calculated, the data points of each convection regime would appear as fully connected lines. As an example, the region from 177 °C to 181 °C is shaded red for later comparisons. The temperature field for two T_h values in this region is displayed in Fig. 1b and c. According to Eq. 2, only 2D convection cells occur at the fault. The onset of a new convection regime leads to a lower energetic state of the system. For instance, the snapshot in Fig. 1b, which has two convection cells, corresponds to $N_s = 1.3$, whereas the snapshot with five convection cells in Fig. 1c has $N_s = 1.1$, even though its T_h value is 2 °C higher.

We evaluate a surrogate model for the temperature field T in Fig. 3, where the hyperparameters of the neural network and POD are shown in Fig. 3c. Note that this is the best obtained result after performing a hyperparameter search using the Tree-structured Parzen Estimator algorithm with 60 trials. In Fig. 3a, the calculated N_s from the surrogate is overlaid on N_s from the full-order solutions for the test and training set. The temperature fields, which serve as the basis for calculating N_s, are illustrated for five representative test samples of T_h in Fig. 17 of the

Fig. 2 Entropy generation numbers N_s of the full-order model training set when varying T_h from 130 °C to 220 °C. The snapshots are taken at 10^{13} s. The colours represent the number of cellular modes. The red-shaded region illustrates an exemplary T_h range where up to four different convection regimes coexist

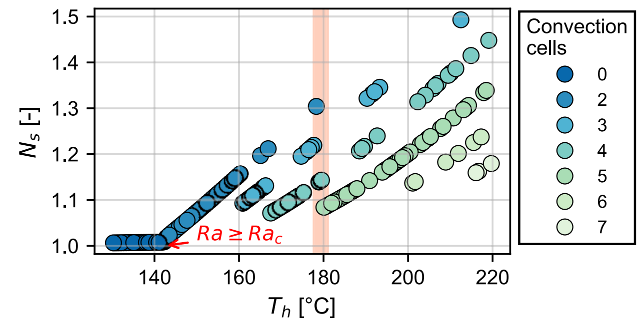

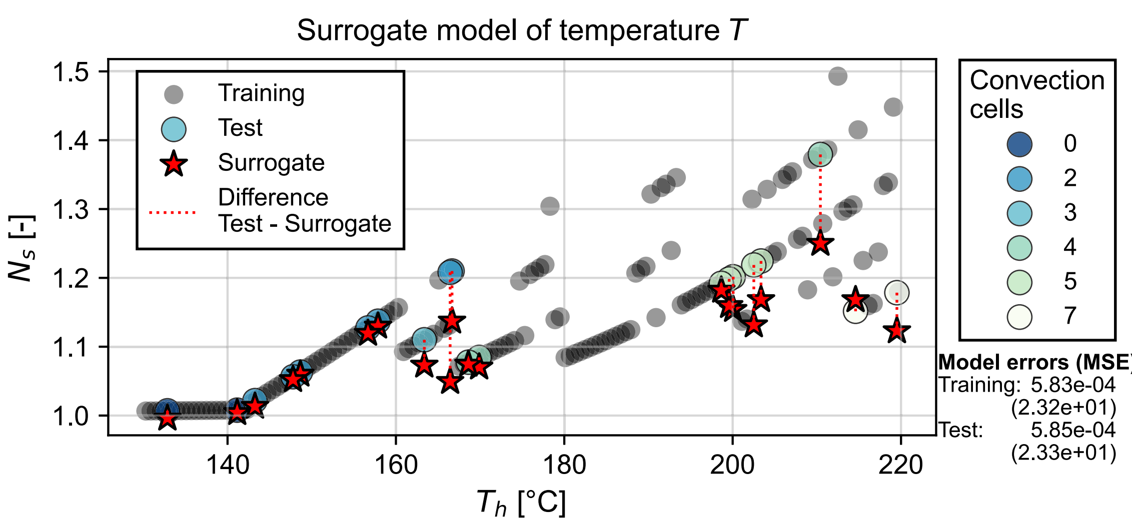

(a)

(b)

(c)

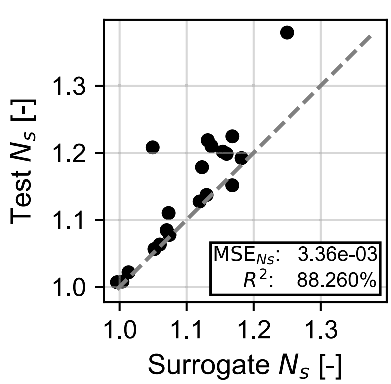

ϵ	99.9999 %
Number of basis functions	28
Scaling features	Z-Score
Scaling output	Mean
Training data	150
Test data	20
Hidden layers	[36, 258, 218, 164, 150, 156]
Activation	Sigmoid
Number of epochs	28499 (Steps 57000, batch size 126)
Learning rate	5.66×10^{-4}
Optimizer	Adam
Max. abs. rel. error	11.6 %

Fig. 3 Results of the surrogate model of the temperature field when varying T_h. (**a**) shows the calculated N_s from the temperature field of the full-order solutions from the training and test data set, as well as from the surrogate model. The lower-right panel shows the MSE for the scaled temperature field T, with the corresponding unscaled values given in brackets in units of $°C^2$. (**b**) shows the correlation between the predicted and test N_s. (**c**) displays the hyperparameters of the neural network and POD

Appendix. A comprehensive comparison across the entire test dataset for all surrogate models evaluated in this study is available in the supplementary material.

It is visually evident in Fig. 3a that the surrogate model's performance decreases as T_h increases. Before the second bifurcation at 160 °C, the predictions align almost perfectly with the full-order solutions. The multistability in the system for $T_h > 160\,°\mathrm{C}$ introduces larger errors to the surrogate solution. Especially when the amount of training data is low for a specific convection regime, the errors can become significant. For example, predictions for seven convection cells are poorly predicted because only three training snapshots exist for this regime (Fig. 2). The MSE for the scaled training and validation datasets are approximately 5.83×10^{-4} and 5.85×10^{-4}, which corresponds to an average error of ca. $4.8\,°C$ per node for the unscaled datasets. The results are obtained with 28 basis functions, indicating a high level of complexity for this idealized problem compared to other benchmark examples [4].

Next, we construct a surrogate model for the entropy generation S'''_{gen} directly, rather than the temperature. Exemplaric snapshots of S'''_{gen} of the red shaded region in Fig. 2 are shown in Fig. 1d and e. Due to its range of up to three orders of magnitude, S'''_{gen} is $\log_{10}$ transformed first before applying any further scaling to it. In the POD

(a)

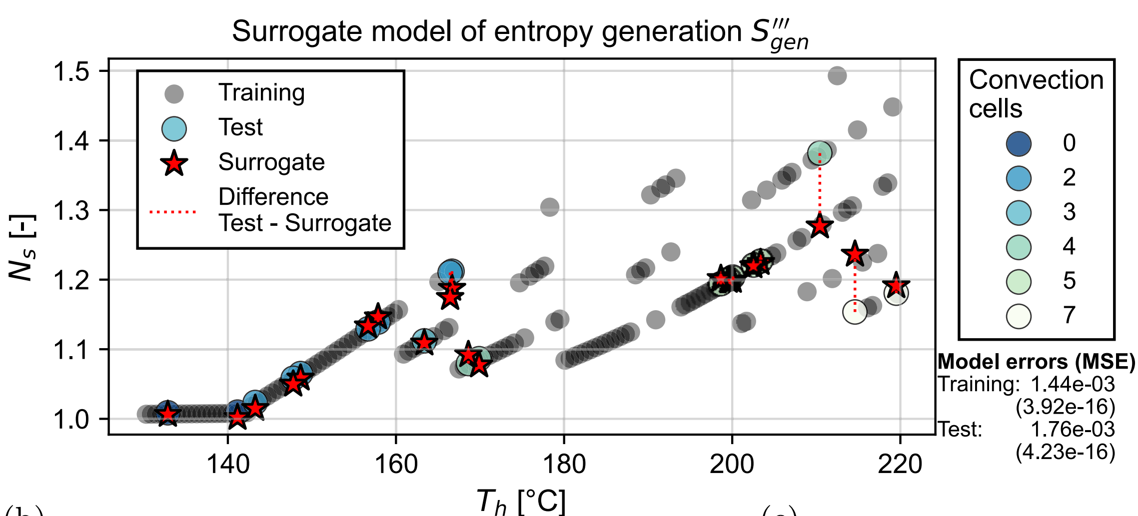

(b)

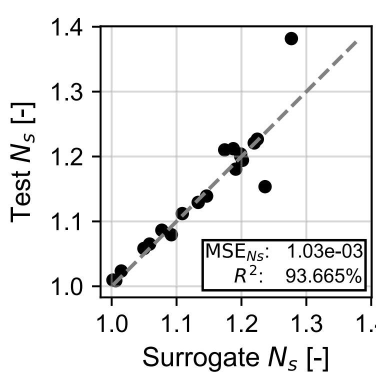

(c)

Tolerance ϵ	99.999 %
Number of basis functions	25
Scaling features	Z-Score
Scaling output	MinMax
Training data	150
Test data	20
Hidden layers	[13, 120, 294, 74, 54]
Activation	Sigmoid
Number of epochs	19333 (Steps 58000, batch size 64)
Learning rate	1.495×10^{-3}
Optimizer	Adam
Max. abs. rel. error $\log_{10}(S'''_{\mathrm{gen}})$	17 %

Fig. 4 Results of the surrogate model of the entropy generation field when varying T_h. (**a**) shows the calculated N_s from the temperature field of the full-order solutions from the training and test data set, as well as from the surrogate model. The lower-right panel shows the MSE for the scaled entropy generation field S'''_{gen}, with the corresponding unscaled values given in brackets in units of $(\mathrm{W\,K^{-1}\,m^{-3}\,s^{-1}})^2$. (**b**) shows the correlation between the predicted and test N_s. (**c**) displays the hyperparameters of the neural network and POD

step, the tolerance is lowered by one order of magnitude to $\epsilon = 99.999\,\%$ compared to the temperature-based surrogate model (Fig. 3c). However, a comparable number of basis functions is extracted: 25 versus 28. The $\log_{10}$ transform of S'''_{gen} impacts the POD step; without it, only 14 basis functions would be extracted. Although the global error of the scaled data set is in the order of 10^{-3} (Fig. 4) and slightly higher than in the surrogate model of the temperature field (order of 10^{-4} in Fig. 3a), the MSE_{Ns} has reduced to 1.03×10^{-3} compared to previously 3.36×10^{-3}. The entropy generation fields S'''_{gen}, used to calculate N_s in Fig. 4, are shown for five representative test samples of T_h in Appendix Fig. 18.

Whereas visual errors were already visible from 160 °C in Fig. 3a, the quality of the predictions in Fig. 4a starts to visually decline from 200 °C. In general, the quality of the predictions has increased: For the entropy generation–based surrogate model, the predicted N_s matches the true values more closely in regions with coexisting convection regimes, particularly between 160 - 170 °C and 195 - 205 °C. In contrast, the temperature-based surrogate model shows greater variance in N_s within these ranges. We elaborate on this further at the beginning of the Discussion. Henceforth, we will utilize surrogate models for S'''_{gen}.

4.2 Reaching insufficient accuracies when multistability cannot be resolved (Varying the dip δ)

In the next example, we vary the dip angle of the fault δ from 55° to 90° while keeping all the other parameters fixed as indicated in Table 1. As the variation of the dip angle leads to different amounts of nodes in the mesh grid, we map the data points onto a uniformly spaced control mesh with a resolution of 100 m. The resolution was chosen as a compromise between the memory consumption of the interpolated data sets and the MSE_{Ns} between the original meshes and the control meshes. By projecting the temperature gradient ∇T directly onto the control mesh, the resulting MSE_{N_s} remains below 5×10^{-5} for a resolution of 100 m. Moreover, the value range of S'''_{gen} is preserved during the projection, since $S'''_{\mathrm{gen}} \propto \nabla T$ (Eq. 10). This is particularly beneficial for consistent data scaling in the offline stage of the surrogate construction.

Unlike T_h, δ is not directly proportional to the Rayleigh number. Since the vertical height H is kept constant, lower dip angles $\delta < 90°$ increase the space for the convective pore-fluid flow to take place and result in a decrease of the gravity component along the fault. These two effects ensure that lower dip angles promote convective fluid flow, thereby reducing $\mathrm{Ra_c}$ [67].

We generate 150 training sets and calculate the respective N_s. As shown in Fig. 5, convection occurs across the entire range of δ. This indicates that Ra consistently exceeds $\mathrm{Ra_c}$ with the flow field transitioning through two to six convection cells.

We evaluate an entropy generation-based surrogate model for 30 test samples in Fig. 6. While the model MSE are in the same order magnitude 10^{-3} as the previous T_h surrogate, the R^2 value is significantly lower at 61 % compared to values higher than 90 % for the T_h surrogates. A possible explanation for the comparable MSE is the substantially increased nodal density resulting from interpolation onto the control mesh, which raises the number of nodes by approximately a factor of four. In contrast to the original mesh, where element sizes increased with distance from the fault plane, the control mesh employs uniform discretization. As the highest variance in entropy

Fig. 5 Entropy generation numbers N_s of the training set when varying δ from 55° to 90°. The snapshots are taken at 1×10^{13} s. The colors represent the number of cellular modes

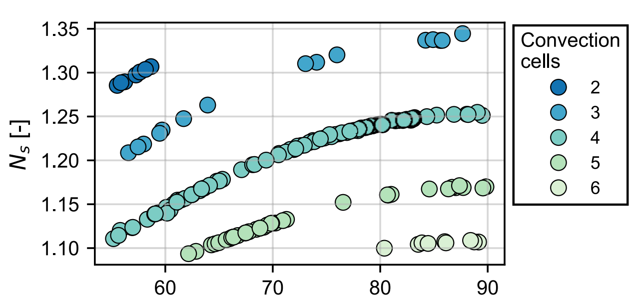

(a)

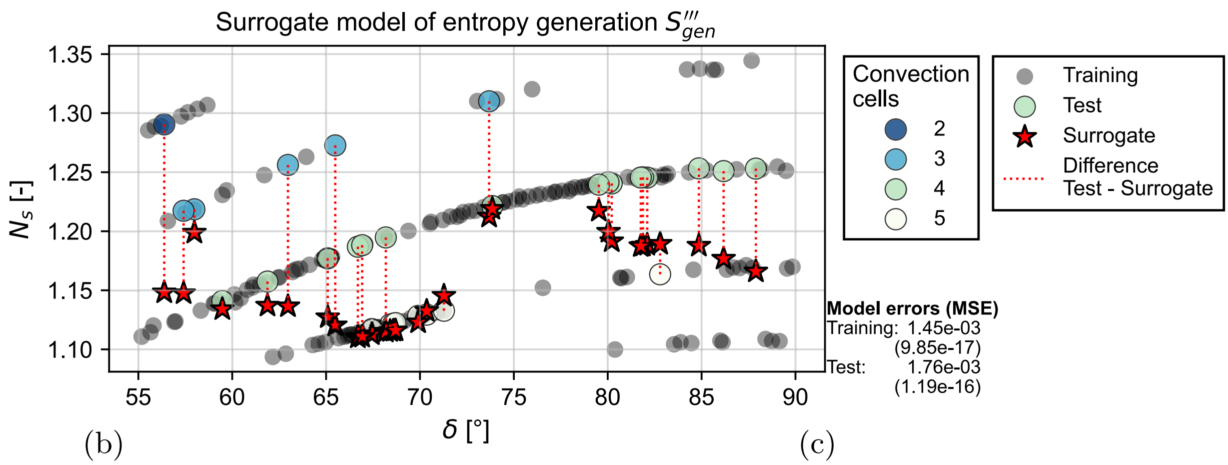

(b)

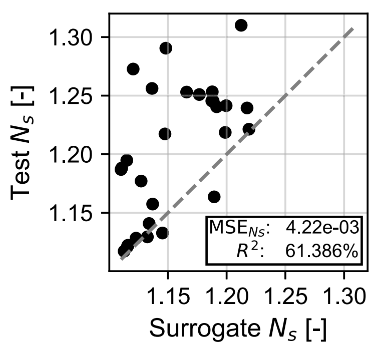

(c)

ϵ	99.999 %
Number of basis functions	147
Scaling features	Z-Score
Scaling output	Mean
Training data	150
Test data	30
Hidden layers	[114, 66, 270, 52, 122, 144]
Activation	Sigmoid
Number of epochs	36749 (Steps 73500, batch size 145)
Learning rate	3.135×10^{-4}
Optimizer	Adam
Max. abs. rel. error $\log_{10}(S'''_{\mathrm{gen}})$	20.7 %

Fig. 6 Results of the surrogate model of the entropy generation field when varying δ. (**a**) shows the calculated N_s from the entropy generation field of the full-order solutions from the training and test data set, as well as from the surrogate model. The lower-right panel shows the MSE for the scaled entropy generation field S'''_{gen}, with the corresponding unscaled values given in brackets in units of $(\mathrm{W\,K^{-1}\,m^{-3}\,s^{-1}})^2$. (**b**) shows the correlation between the predicted and test N_s. (**c**) displays the hyperparameters of the neural network and POD

generation — and consequently the most significant prediction errors — arises in the proximity of the fault plane, the mesh refinement primarily introduces additional regions with comparatively small errors outside convection-driven temperature anomalies. This redistribution of error reduces the MSE, which reflects a domain-averaged metric.

Additionally, 147 basis functions are chosen, reflecting the high complexity of the system and approaching the 150 training snapshots, which indicates that the whole problem's complexity is not entirely captured. However, additional training snapshots were not generated because the underlying complexity arises from the solution ambiguity: overlapping solutions occur across nearly the entire dip range, whereas the overlap for varying T_h was more localized between 160 °C to 220 °C. In the next section, we will introduce the concept of physical preconditioning to circumvent this issue. Consequently, during training of the surrogate model, no clear relationship between δ and the reduced basis coefficients θ could be found in the machine learning step. This ambivalence causes most predicted values to fall between the trajectories associated with each convection regime. In addition, specific convection regimes are represented by only a limited number of training samples (e.g., for two or six convection cells). Between dips of 65° to 70°, the dominant solution corresponds to five convection cells, whereas between 70° to 80°, the preferred solution shifts to four cells. Test cases outside these ranges are never predicted correctly. Consequently, the surrogate fails to make reliable predictions of S'''_{gen}.

(a) Same parameter samples as in Fig. 2 (b) Same parameter samples as in Fig. 5

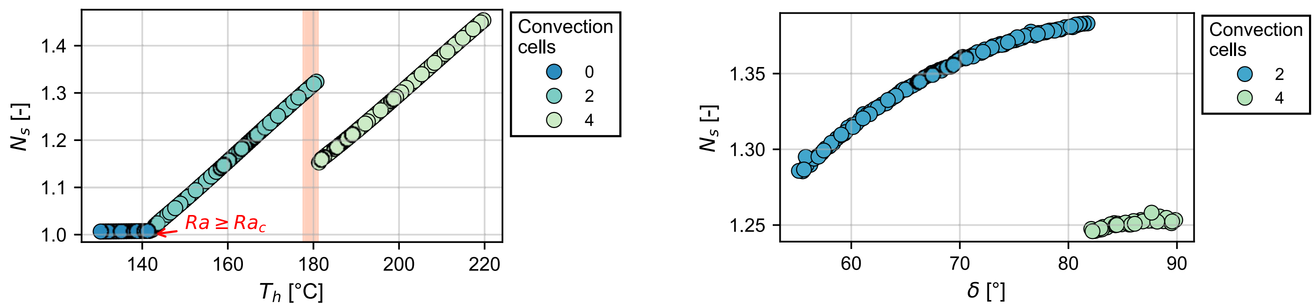

Fig. 7 Entropy generation number N_s of the training data set with physical preconditioning (Eq. 9). The red-shaded region in (**a**) marks the same range as in Fig. 2

4.3 Reducing the number of bifurcations by physical preconditioning

As seen in the previous section, multisolutions, where different convection regimes coexist for the same parameters, might lead to significant inaccuracies in the surrogate model. A suitable choice of temperature ICs can reduce the number of bifurcations, thereby placing the system closer to the basin of attraction of a specific solution [22]. For example, the IC of the Elder Problem were placed close to the border of the basin of attraction of two solutions, which made the numerical simulation extremely sensitive to any perturbation [68].

In the case of the idealized scenario in this study, each of the induced multicellular configurations of Eq. 9 will become an equilibrium state solution provided this solution is stable and exists. As we consider a planar fault, we set $m = 0$, $n = 2$, and $A = 1$ to start with one upwelling in the center of the fault. The final IC is obtained by superimposing Eq. 9 on the constant temperature gradient between T_0 and T_h. Re-evaluating the same training and test parameter sets of T_h and δ from Figs. 2 and 5 shows that the variance in the convection regimes is reduced (Fig. 7). In the case of T_h (Fig. 7a), equilibrium state solutions with only two or four convection cells are observed. Onset of convection starts at $T_h \approx 143$ °C, consistent with the previous example in Fig. 2. However, only one additional bifurcation is found at approximately 181 °C, leading to four convection cells. The red shaded region denotes the same region as in Fig. 2 for reference. In this model, a clear progression from two to four convection cells is visible.

For varying δ (Fig. 7b), the convection regimes are also restricted to two or four cells, with a bifurcation at 82°. In contrast, two-cell solutions only appeared between 55° to 60° in Fig. 5. In summary, adding Eq. 9 with $n = 2$ results in two convection cells until the solution is no longer physically possible, at which point the bifurcation occurs.

Next, we construct surrogate models with the training sets in Fig. 7. The results for varying T_h are shown in Fig. 8. Compared to using a constant geothermal gradient as IC, the MSE for the training and test sets decreased by four and three orders of magnitude, respectively. Consequently, the surrogate and full-order model solutions are visually indistinguishable. To evaluate the surrogate model's performance across different convection cells at comparable N_s values, five additional test samples were added within the T_h range of 175 °C to 195 °C (cyan stars in Fig. 8a). Also, only eight basis functions are extracted in the POD step, compared to 25 in Fig. 4, indicating the reduced complexity of the problem.

Similarly, the surrogate model for varying δ performs better when perturbed ICs are applied (Fig. 9). Training MSE decreases by two orders of magnitude and test MSE by one order of magnitude, while R^2 improves from 61 % to 93 %. The number of basis functions decreases slightly, from 147 to 133, indicating that a variable dip angle introduces substantial complexity into the system, largely independent of the chosen IC. Nevertheless, most surrogate solutions remain visually indistinguishable from the full-order solutions. An exception occurs for the two test samples located near the bifurcation point at 82°, where errors are anomalously high. Without these two test

 https://doi.org/10.1007/s10596-026-10421-w

(a)

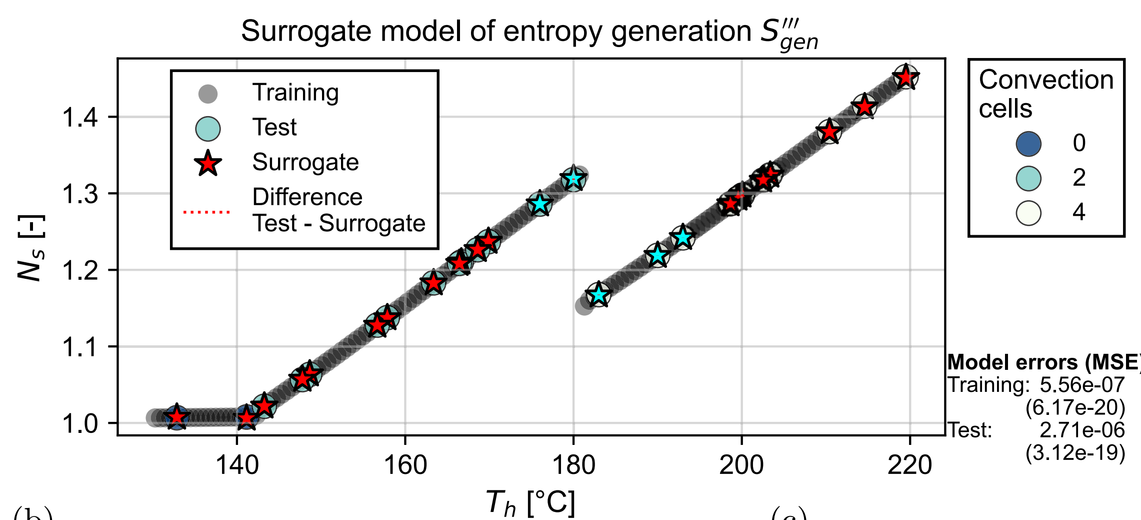

(b)

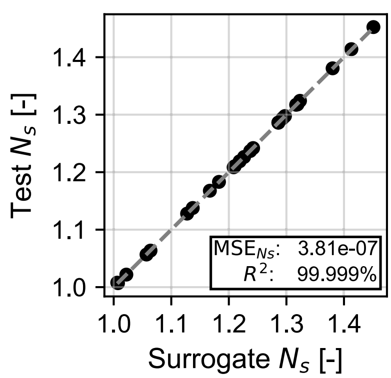

(c)

ϵ	99.999 %
Number of basis functions	8
Scaling features	Min Max
Scaling output	Min Max
Training data	150
Test data	25
Hidden layers	[13, 152, 122, 162, 152, 72]
Activation	Sigmoid
Number of epochs	44999 (Steps 90000, batch size 106)
Learning rate	1.243×10^{-3}
Optimizer	Adam
Max. abs. rel. error $\log_{10}(S'''_{\mathrm{gen}})$	0.5 %

Fig. 8 Results of the surrogate model of the entropy generation field when varying T_h after physical preconditioning. (**a**) shows the calculated N_s from the entropy generation field of the full-order solutions from training and test data, as well as from the surrogate model. The lower-right panel shows the MSE for the scaled entropy generation field S'''_{gen}, with the corresponding unscaled values given in brackets in units of $(\mathrm{W\,K^{-1}\,m^{-3}\,s^{-1}})^2$. (**b**) shows the correlation between the surrogate and test N_s. (**c**) displays the hyperparameters of the neural network and POD

samples, the test MSE is 5.0×10^{-5} compared to 1.4×10^{-4} and MSE$_{N_s}$ improves by two orders of magnitude to 3×10^{-6} with R^2 being 99.94 %, showing that the inaccuracies are mainly related to the two test samples. Consequently, even with suitable ICs, ambiguities persist in the vicinity of bifurcation points.

4.4 Transition to oscillatory convection regimes (Varying k_F)

Similar to T_h, the fault permeability k_F is directly proportional to Ra (Eq. 7) and directly influences the convective behavior of the system. From a geological point of view, it exhibits greater variability than T_h, potentially spanning over several orders of magnitude across multiple scales, particularly at faults [41, 62]. We construct a surrogate model considering varying k_F ranging from 5×10^{-15} m^2 to 1×10^{-12} m^2 and evaluate N_s of the training data in Fig. 10, where Ra$_\mathrm{c}$ is reached at approximately 8×10^{-14} m^2. For clarity, we plot N_s for k_F starting at 5×10^{-14} m^2, since all solutions below 8×10^{-14} m^2 remain in the conductive regime. The second and third bifurcations occur at 2.5×10^{-13} m^2 and 2.9×10^{-13} m^2, corresponding to the formation of three and four convection cells in an equilibrium state regime. To illustrate this, the phase space of the transient simulation for

(a)

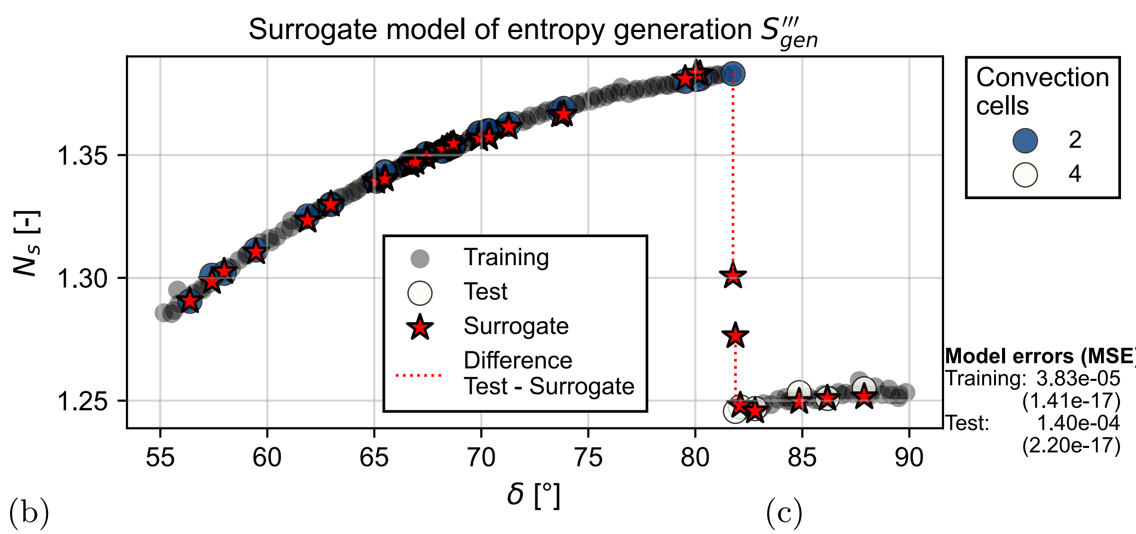

(b)

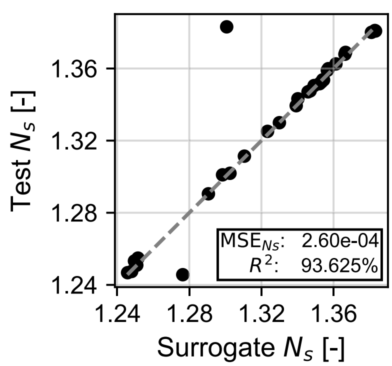

(c)

ϵ	99.999 %
Number of basis functions	133
Scaling features	Min Max
Scaling output	Min Max
Training data	150
Test data	30
Hidden layers	[39, 56, 136, 146]
Activation	Sigmoid
Number of epochs	19999 (Steps 180000, batch size 18)
Learning rate	9.412×10^{-5}
Optimizer	Adam
Max. abs. rel. error $\log_{10}(S'''_{\mathrm{gen}})$	21.0 %

Fig. 9 Results of the surrogate model of the entropy generation field when varying δ after physical preconditioning. (**a**) shows the calculated N_s from the entropy generation field of the full-order solutions from training and test data, as well as from the surrogate model. The lower-right panel shows the MSE for the scaled entropy generation field S'''_{gen}, with the corresponding unscaled values given in brackets in units of $(\mathrm{W\,K^{-1}\,m^{-3}\,s^{-1}})^2$. (**c**) displays the hyperparameters of the neural network and POD

a sample with two convection cells at $k_F = 2.0 \times 10^{-13}$ m^2 is shown in Fig. 11a, where N_s is plotted against its temporal derivative at each time step of the solver. The color of the points indicates the simulation time, with brighter colors indicating later times. Due to the imposed IC and the initial time step of 5×10^{-2} s, a peak appears at the start of the transient simulation. This peak disappears once fluid motion generates a thermal upwelling for

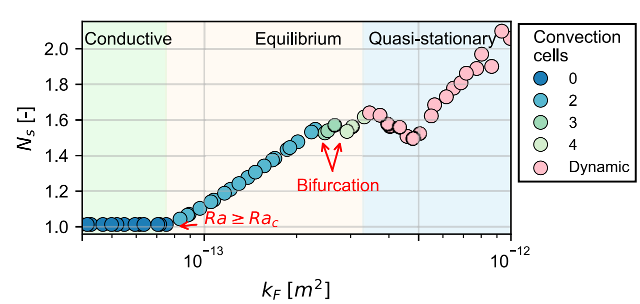

Fig. 10 Training samples when varying k_F from 1×10^{-15} m^2 to 1×10^{-13} m^2. Note that the x-axis is cut for visualization purposes. The snapshots are taken at 1×10^{13} s for the equilibrium state solutions and at 2×10^{11} s for the dynamic solutions

 https://doi.org/10.1007/s10596-026-10421-w

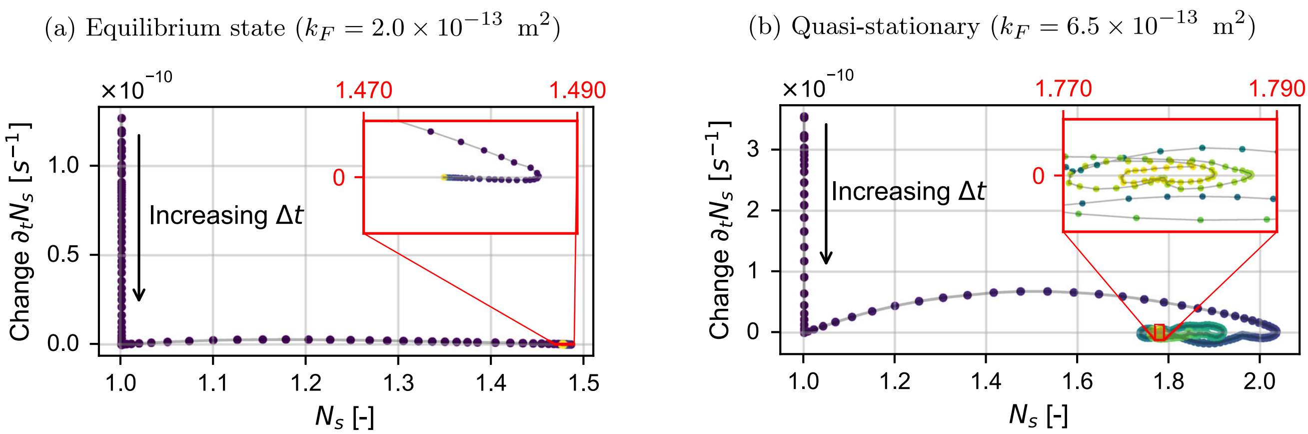

Fig. 11 Phase space of two training samples in Fig. 10. The color of each point denotes the simulation time, with brighter colors indicating later times. The red boxes show a detailed view of a selected region

increasing solver time steps. The onset of convection starts when $N_s > 1$. In the phase space, the orbit moves toward an attractor at ($N_s \approx 1.477$, $\partial_t N_s = 0$) and remains there.

In contrast, no equilibrium state solutions exist for $k_F > 3.5 \times 10^{-13}$ m^2, implying that the temporal variation of N_s is not constant. In Fig. 10, which shows the relationship of k_F with N_s at the last time step, no clear relationship can be inferred. Also, labeling the convection cells was omitted due to unstable convective fingers appearing at the bottom edges of the fault plane. However, the phase space of a transient simulation for $k_F = 6.5 \times 10^{-13}$ m^2 in Fig. 11b reveals that the orbit behavior corresponds to a quasi-stationary solution because the model orbits a basin of attraction at N_s between 1.77 and 1.79. The positive and negative temporal changes of N_s correspond to oscillations between higher and lower energetic states of the system. The simulations were first run up to 2×10^{11} s to identify quasi-stationary regimes, which require more computation time than equilibrium state regimes because we use an implicit solver with backward differentiation formulas and automatic time-step selection. The equilibrium state solutions were run 10^{13} s to ensure convergence. Consequently, the training snapshots show both equilibrium state solutions at 10^{13} s with clear bifurcation points and quasi-stationary solutions at 2×10^{11} s.

Next, we construct a surrogate model using the training samples from Fig. 10 and physical preconditioning, with the results shown in Fig. 12. Due to the value range over several orders of magnitude, the k_F values are $\log_{10}$ transformed first before any further scaling. Compared to the model with varying T_h (Fig. 8), which required eight basis functions, this case extracts 28 basis functions, reflecting the higher complexity of the problem. While only two and four equilibrium state convection cells were observed in the T_h case, varying k_F introduces three distinct equilibrium state regimes as well as a quasi-stationary regime. The training and test MSEs are 8.9×10^{-5} and 2.3×10^{-4}, respectively. This higher complexity likely explains the reduced performance, with test errors about two orders of magnitude larger than in the T_h surrogate. The largest local errors occur in regions where unstable convective fingering develops. Nevertheless, the surrogate model successfully captures the different convection regimes, achieving an R^2 of 99.93 % and an MSE$_{N_S}$ of 2.2×10^{-4}.

4.5 Varying multiple parameters

Finally, we will vary all free parameters listed in Table 1. To remain within the scope of this study - focusing on the construction of surrogate models for convection-dominated systems - δ will not be varied. The simulation time was set to 2.5×10^{12} s to avoid excessive computation times once a quasi-stationary state is reached, as we employ an implicit solver with backward differentiation formulas and automatic time step selection. The N_s values of the training snapshots are displayed for the previously examined parameters T_h and k_F in Fig. 13 while the results for the remaining parameters are provided in the supplementary material.

(a)

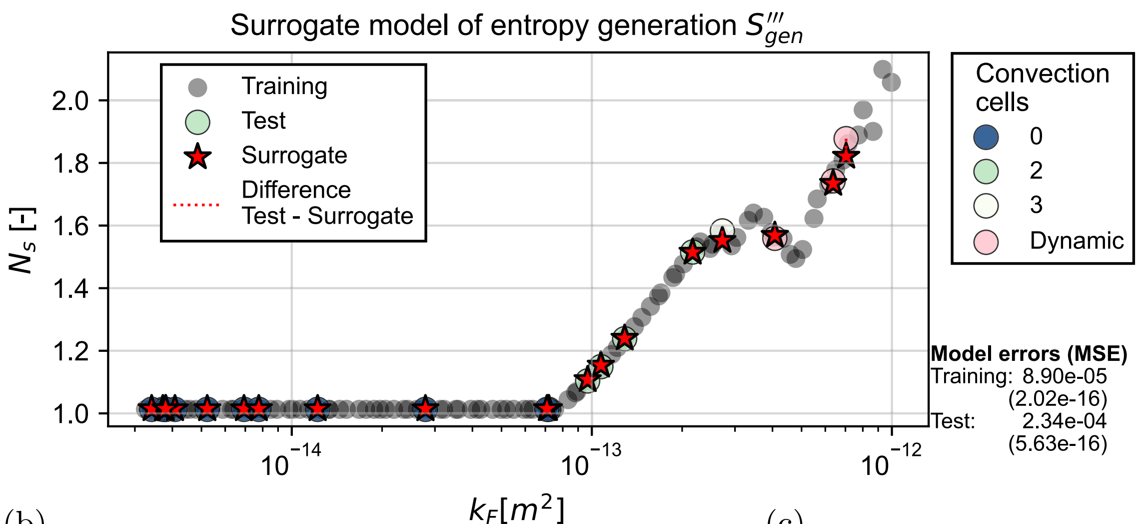

(b)

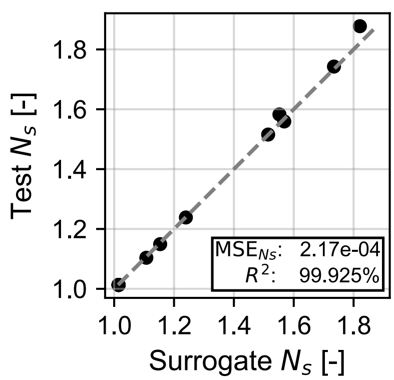

(c)

ϵ	99.999 %
Number of basis functions	28
Scaling features	Z-Score
Scaling output	Mean
Training data	100
Test data	20
Hidden layers	[3, 248, 76, 252, 168, 260]
Activation	Sigmoid
Number of epochs	33749 (Steps 67500, batch size 69)
Learning rate	8.857×10^{-4}
Optimizer	Adam
Max. abs. rel. error $\log_{10}(S'''_{\mathrm{gen}})$	20.9 %

Fig. 12 Results of the surrogate model of the entropy generation field when varying k_F after physical preconditioning. (**a**) shows the calculated N_s from the entropy generation field of the full-order solutions from training and test data, as well as from the surrogate model. The lower-right panel shows the MSE for the scaled entropy generation field S'''_{gen}, with the corresponding unscaled values given in brackets in units of $(\mathrm{W\,K^{-1}\,m^{-3}\,s^{-1}})^2$. (**b**) shows the correlation between the surrogate and test N_s. (**c**) displays the hyperparameters of the neural network and POD

(a) (b)

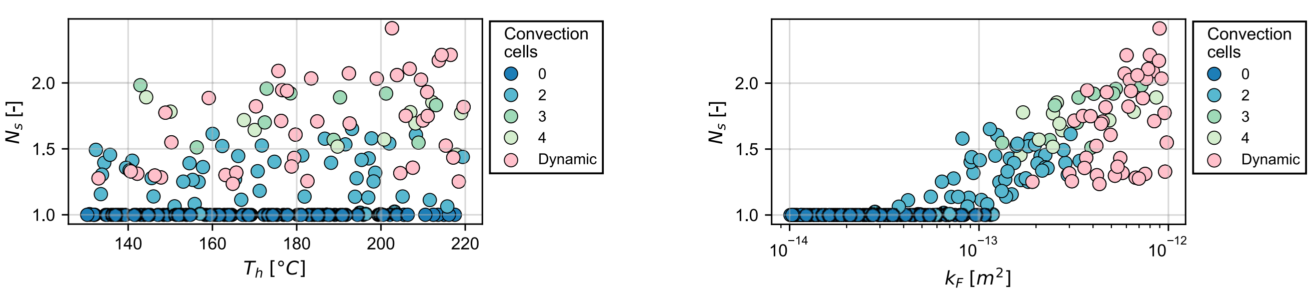

Fig. 13 Entropy generation numbers of training samples when varying parameters in Table 1 except δ for the last time step at 2.5×10^{-12} s

 https://doi.org/10.1007/s10596-026-10421-w

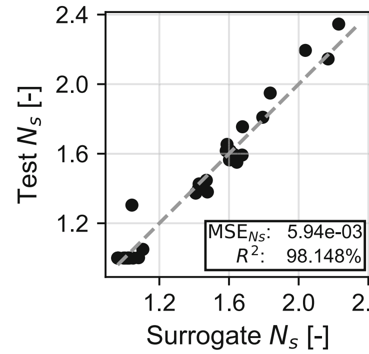

Fig. 14 Predicted versus true test entropy generation number N_s of the surrogate model when varying multiple parameters

Within the observed N_s range (1.0 to 2.4), conductive regimes, onset of convection towards a steady-state, equilibrium state convection, and quasi-stationary (dynamic) regimes exist. The majority of the snapshots show an equilibrium state with two convection cells or a quasi-stationary regime, whereas only 10 and 11 samples show three and four convection cells. This may affect predictions of convection regimes for which fewer training snapshots are available, as seen in the initial example for varying T_h. Unlike in previous simulations, no clear bifurcation points are visible due to the simultaneous variation of multiple parameters, even with physical preconditioning.

In total, 200 training and 30 test snapshots are computed. The POD step with a 99.999 % tolerance ϵ yields 52 basis functions when using the min-max normalization. The scaled model MSEs of $\log_{10}(S'''_{\text{gen}})$ are 1.1×10^{-3} and 1.2×10^{-3} for training and test samples with a maximum local error of 26 %. The metrics of the test set for true and predicted N_s are shown in Fig. 14: Whereas the MSE_{N_s} is the highest obtained (5.94×10^{-3}) in all surrogate models so far, the R^2 value of 98 % indicates a high predictive performance of the surrogate. The highest deviation occurs for a "false negative" sample, where convection occurs ($N_s = 1.3$) but is not predicted by the surrogate ($N_s = 1.0$). For this sample, $T_h = 131\,°\text{C}$ lies at the lower limit of the range and $k_F = 6.5 \times 10^{-13}$ m^2 at the upper limit, indicating that the training set may not adequately cover this combination. However, the surrogate produces reliable predictions for this study.

4.6 Comparing computation times

The minimum simulation time in COMSOL Multiphysics® of the last presented model is approximately two minutes for the conductive solution. The longest simulation time took over 1000 minutes for highly convective solutions due to the adaptive time stepping (12th Gen Intel® Core™ i7-12700 2.10 GHz,64 GB RAM, using 5 of 20 cores). Evaluating the 30 test samples during the online stage of the surrogate model took approximately 1 ms, which results in speed-ups from 10^4 to 10^7. The training for the optimal neural network took ca. 30 minutes. During hyperparameter optimization, ca. 50 neural networks are generated whose training time took between 10 and 60 minutes, depending on the hyperparameters.

To demonstrate the utility of surrogate models, we calculate the expected computation times for a global sensitivity analysis (SA). This analysis explores how variations of uncertain input parameters impact the quantity of interest N_s [69]. Depending on the objective, SA can help to identify where additional data acquisition can reduce uncertainty and how to simplify the model's complexity. Also, they can rank parameter influence, thereby revealing dominant physical processes and enhancing model understanding [70]. Conducting a Sobol SA for this model would require approximately two million samples, using 2^{17} evaluations per parameter [71, Theorem 2]. Uncertainty quantifications typically require thousands to millions of forward computations as well [10, 72]. Assuming an average simulation time of 10 minutes with the finite element solver, two million evaluations require approximately 38 core-years (computation time). In contrast, the same evaluations during the online stage of the surrogate would be approximately 33 minutes. Parallel computing can further reduce the evaluation time, as sensitivity analyses can be fully parallelized. Moreover, calculating the quantity of interest N_s can further increase the computation time, since it involves integrating the entropy generation field S'''_{gen}.

5 Discussion

Within this study, we present how physics-based machine learning can be used to construct reliable surrogate models for predicting the thermal state of an idealized fault system. We discuss how the surrogate performance can be enhanced by reducing physical complexity through physical preconditioning and using entropy generation as a measure. Next, we examine the implications of our results for real-world applications and how analyzing N_s helps characterize the system. Finally, we highlight the limitations of this study and outline potential future research directions.

5.1 Implications for surrogate modeling of convective systems

Constructing surrogate models for the entropy generation field S'''_{gen}, rather than the temperature field T, yielded slightly better results. The coexistence of different solutions - regions with overlapping N_s for the same configuration, similar to the Elder problem [68] - can lead to difficulties during the surrogate model construction.

The equilibrium state solutions for varying T_h were better predicted by entropy generation-based surrogate models than by those based on temperature, up to a temperature of approximately 210 °C, even without physical preconditioning. In contrast to T, S'''_{gen} can vary over several orders of magnitude (Fig. 1e). The $\log_{10}$ transformation, applied before any further scaling, can compensate for most of the unequal scaling. In the POD step, the entropy generation field extracted a number of basis functions similar to the temperature field, despite a lower tolerance ϵ. Since calculating S'''_{gen} depends on the temperature gradient, it is unsurprising that each POD mode captures a different amount of the system's energy.

We observed that physical preconditioning can substantially enhance the performance of surrogate models. This approach, used to force a specific family of solutions in convective systems, has also been applied by other authors [46, 73]. However, it comes at a cost: changing the IC can potentially hide some physically possible solutions from the practitioner. For instance, modifying the IC for varying T_h produced only two or four convection cells (Fig. 7a), whereas without such perturbations, the same parameters could yield between two and seven cells (Fig. 2). These observations highlight the importance of a stochastic perspective when modeling free convection, particularly when no prior information about the temperature field is available. As noted by Xie et al. [74], free convection processes inherently allow multiple physically plausible solutions, including bifurcating and oscillatory patterns, which a single deterministic simulation cannot capture. Introducing random perturbations to ICs expands the range of possible outcomes and helps account for this variability. Horne and Caltagirone [75] pointed out that mathematical solutions to non-linear problems should include nondeterministic forcing to avoid results that are correct mathematically but unlikely physically. Surrogate models have a particular potential in this context, as they enable stochastic analyses of physical processes due to significant speed-ups [4]. To fully explore the solution space, one promising approach could be to treat the wave numbers m and n from the perturbation function (Eq. 9) as additional inputs to $\vec{\mu}$, allowing the surrogate to capture all potential solution branches.

In this study, the IC from Eq. 9 was applied to the entire 3D domain, even though convection is expected to occur only along the fault. Ideally, the IC would be prescribed only on the fault itself. However, COMSOL Multiphysics® does not allow initial temperature conditions to be assigned explicitly to surfaces. We assume that applying them to the full domain does not affect the results and yields behavior equivalent to prescribing them only at the fault.

A key advantage of surrogate modeling lies in the substantial computational savings achieved by using surrogate models instead of full-order model evaluations. Solving convection scenarios with the full-order model requires minutes for equilibrium state solutions and up to hours for quasi-stationary solutions due to adaptive time-stepping. In contrast, evaluating the surrogate takes only milliseconds, resulting in a speed-up of up to seven orders of magnitude. This comparison excludes the offline training stage. However, when the objective is to perform global sensitivity or uncertainty analyses involving millions of forward simulations [69, 70], the benefits become immediately apparent.

Although parameter ranges in real-world applications may be more restricted than those listed in Table 1, similar phenomena to those observed in this study can still arise. While ideal periodic patterns can be generated in experiments, natural convective patterns are typically disordered [76]. Nevertheless, assumptions made in many applications of numerical modeling can lead to stationary convection patterns [34, 77–81], which may lie close to bifurcation points. When constructing a surrogate model, it is therefore crucial to identify such points to make a well-informed evaluation of the surrogate's performance. Even with physical preconditioning, the surrogates exhibited their most significant errors in the vicinity of these bifurcation points, which is unavoidable. Around the bifurcation point, no surrogate model (independent of the technique) will result in a reliable model. This is not only a physical effect but is also largely increased by the numerical instability around these points. For parameter spaces with higher dimensions, identifying bifurcation points may help identify local points of degraded quality. While this study uses a box, in reality, the potentially convective layer will have a much smaller aspect ratio, which reduces the likelihood of convection. This study highlights the importance of investigating faults, which in real-world scenarios represent likely locations for convection [17, 80, 82]. This entails a more favorable condition for the surrogate models in real-case scenarios.

As evaluating entropy generation may seem like an abstract concept, it can be helpful to examine the effect of temperature uncertainties on the entropy generation. To explore this, we randomly introduced positive and negative temperature perturbations to representative full-order snapshots from our study and computed the resulting maximum absolute relative error on $\log_{10}(S'''_{\text{gen}})$, shown in Fig. 15. Across the entropy generation-based surrogate models, the maximum observed local errors were approximately 25 % for $\log 10(S'''_{\text{gen}})$, corresponding to temperature inaccuracies of around 1 K to 2 K. Considering that true in-situ temperature measurements are affected by uncertainties of up to several Kelvin [83], the approximation errors from the surrogate are in the same order of magnitude. From Eq. 10 and Fig. 15, a power-law relationship between temperature inaccuracies and local errors in entropy generation can be inferred. For instance, if the maximum local errors are reduced to 15 % or 10 %, this would correspond to temperature uncertainties of roughly ± 0.5 K and ± 0.1 K, respectively. Achieving lower error levels may be possible in real-world scenarios with more restricted parameter ranges or under equilibrium conditions.

N_s is a highly informative quantity of interest for TH systems, as it captures both the thermal and hydraulic components (Eq. 10). It can be used to address epistemic uncertainties as demonstrated by Santoso et al. [84] in a sensitivity analysis of a TH model of The Hague, Netherlands. Additionally, when combined with information entropy, it serves as a valuable metric for interpreting and comparing uncertainties in the modeled subsurface geology and simulated flow fields [85]. However, we only used the thermal contribution and ignored the viscous

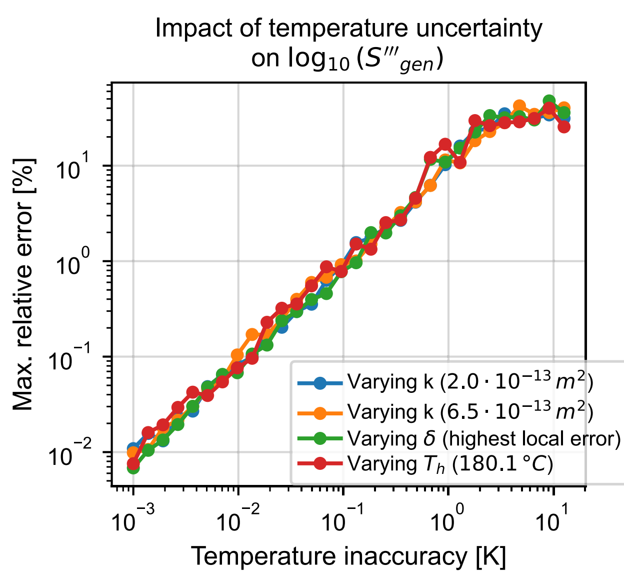

Fig. 15 Maximum absolute relative error when comparing the entropy generation from the full-order temperature field with and without randomly added temperature uncertainties. The blue and orange lines correspond to the last time step of Fig. 11. The green line is the test dataset with the highest local error (21 % at $\delta = 68.4$ ° in Fig. 7b). The red line corresponds to Fig. 1d

dissipation in this study. Evaluating the entropy generation numbers $N_{s,\mathrm{visc}}$ for the equilibrium and quasi-stationary state in Fig. 11 yielded 0.02 and 0.05, respectively, compared to their thermal contribution 1.48 and 1.79. This results in a Bejan number of 98.7 and 97.2 %. Thus, viscous dissipation has a negligible contribution to the total entropy generation, especially in homogeneous media and when considering realistic viscosity ranges of water [29]. However, if low-permeability heterogeneities block preferred convective flow paths, viscous dissipation can play a larger role [30, 46]. Also, when systems exhibit a combination of forced and natural convection, viscous dissipation should not be neglected [86].

The evaluation of the N_s has proven to provide additional information about the system. Its calculation from S'''_{gen} is straightforward (Eq. 12), and it can help to identify bifurcation points of equilibrium solutions. In this study, N_s values showed a clear dependency on the parameters. At the bifurcation point, the transition to a pattern with a higher wavelength resulted in a sudden jump towards a lower N_s. This observation stands in contrast with Börsing et al. [29], who found a jump towards a higher N_s when a solution exists for a higher wavelength pattern while keeping the aspect ratio and temperature gradient fixed. One reason could be the use of the characteristic entropy generation using isoflux BC (Eq. 11) introduced by dummy layers instead of isothermal ones. Moreover,

(a)

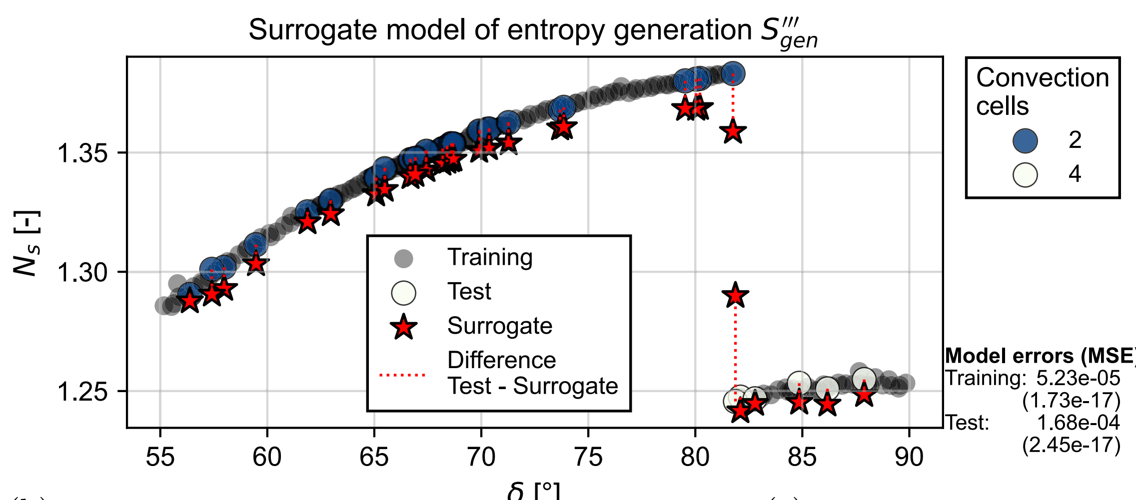

(b)

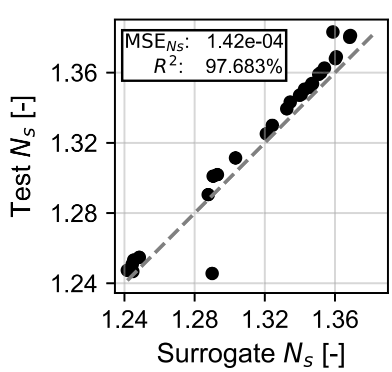

(c)

Scaling features	Z-Score
Scaling output	Min Max
Training data	150
Test data	30
Feature	1
Labels	85731
Hidden layers	[93, 230, 156, 82, 238]
Activation	Sigmoid
Number of epochs	1999 (Steps 4000, batch size 85)
Learning rate	1.275×10^{-3}
Optimizer	Adam
Max. abs. rel. error $\log_{10}(S'''_{\mathrm{gen}})$	21.0 %

Fig. 16 Results of the surrogate model for the entropy generation field when varying δ using a purely data-driven approach compared to Fig. 9. (**a**) Shows the calculated N_s from the temperature field of the full-order solutions from training and test data and from the surrogate model. The lower-right panel shows the MSE for the scaled entropy generation field S'''_{gen}, with the corresponding unscaled values given in brackets in units of $(\mathrm{W\,K^{-1}\,m^{-3}\,s^{-1}})^2$. (**b**) shows the correlation between the predicted and test N_s. The box shows the MSE and correlation coefficient. (**c**) displays the hyperparameters of the neural network

the simulations were performed in a 2D medium. In a 3D medium, the heat flux towards the host rock will be higher when the energetic state is distributed in fewer convection cells, which results in a higher N_s.

5.2 Comparison to data-driven surrogate models

Data-driven surrogate models, although widely used [8, 11, 87], can exhibit disadvantages compared to physics-based approaches. To highlight these differences, we construct an additional surrogate model for the case of a varying dip angle δ, with the training data shown in Fig. 7b. We employ a neural network (NN) that directly maps the parameter $\vec{\mu}$ to S'''_{gen} of each node of the 3D mesh, with the results presented in Fig. 16. The training and test MSEs (5.23×10^{-5} and 1.68×10^{-4}) are comparable to those of the NI-RB surrogate, and both approaches show maximum local errors of 21 % on the test dataset. Similar to NI-RB, the largest errors occur near the bifurcation point at 82°. Excluding the two samples responsible for these peak errors, the training and test MSE reduce to 5.2×10^{-5} and 5×10^{-5}, respectively. The training error is thereby one order of magnitude larger than the NI-RB approach, while the test error remains unchanged. The corresponding R^2 is 99.89 %. As Degen et al. [66] emphasized, analyzing the differences between full-order and surrogate solutions can help address their respective qualities. When they compared predicted versus true stress distributions along depth, the differences for NI-RB appeared as straight lines, whereas the NN produced mostly straight lines with superimposed oscillations. This reflects the fact that the NN yields results that statistically vary around the physical response, while the NI-RB approach remains physically interpretable. In particular, NI-RB has proven to guarantee the scientific requirements of scalability, interpretability, generalizability, and robustness for surrogate models [4, 88].

The differences between the NN and NI-RB are also visible when evaluating the predicted and true N_s in Fig. 16b. Unlike the NI-RB surrogate, where the points mainly lie on the identity line (Fig. 9b), the NN results are slightly shifted, consistent with the oscillatory behavior reported in Degen et al. [66]. This observation further suggests that using N_s as an additional performance metric might be suitable for 3D models, where assessing local differences can be complicated due to large-scale geometries.

5.3 Limitations

In this study, we represented the fault as a lower-dimensional interface, which is a reasonable assumption when fluid flow follows the fault plane [35]. In this implementation, convection is constrained to 2D circulation cells within the fault plane. Nevertheless, both 2D and 3D modes of thermal convection can coexist at fault zones [18, 24]. Implementing a fully 3D fault core and damage zone would enable the investigation of interactions between topography- and thermally-driven flows within permeable units, such as helicoidal flow patterns [24]. Also, in natural systems, fluid dynamics often result from a combination of forced and free convection [16, 18, 89]. Previous studies have shown that the onset of convection in heterogeneous geologic media is highly sensitive to variations in the standard deviation of the lognormal permeability field [90]. Furthermore, depth- and time-dependent variations in permeability can significantly influence the convection patterns at fault zones [23]. Finally, while neglecting viscous dissipation in S'''_{gen} is justified for this study, it should be considered in future work, particularly in systems with forced convection driven by a hydraulic gradient. Also, the NI-RB shows its full potential when considering time-dependent problems. Then, a reduction takes place in both the temporal and spatial dimensions when performing the POD step [66]. Evaluating surrogate model performance under such conditions can be an interesting task for future research.

6 Conclusion

We present multiple approaches to efficiently construct surrogate models of a fault zone-host rock system that includes natural convection. While the benefits in the form of speed-ups of several orders of magnitude are apparent, hidden challenges arise from the coexistence of multiple solutions and transitions to dynamic, quasi-stationary convective regimes. In the following, we highlight key considerations when developing surrogate models for convective geothermal systems:

- Depending on the application, building the surrogate for the entropy generation field S'''_{gen} may provide more robust results than a temperature-based surrogate. Since S'''_{gen} captures both thermal and hydraulic effects, it can serve as a comprehensive indicator for evaluating epistemic uncertainties that can be directly computed from the surrogate.
- The evaluation of the entropy generation can help identify bifurcation points, where surrogate performance typically deteriorates. Recognizing these regions can explain - and potentially mitigate - model limitations.
- Exploring the phase space of the entropy generation number N_s can help to identify stationary, quasi-stationary, and chaotic states of the system.
- N_s can be a suitable additional metric to evaluate the performance of the surrogate.
- Free convection processes inherently allow multiple physically plausible solutions, including bifurcating and oscillatory patterns, which might require a stochastic evaluation of the system instead of a deterministic one. When no prior information about the system is available, the incorporation of the perturbation parameters m, n to the parameter space $\vec{\mu}$ of the surrogate model might help explore all possible solution branches with the surrogate model.

Appendix A: Test data Fig. 3

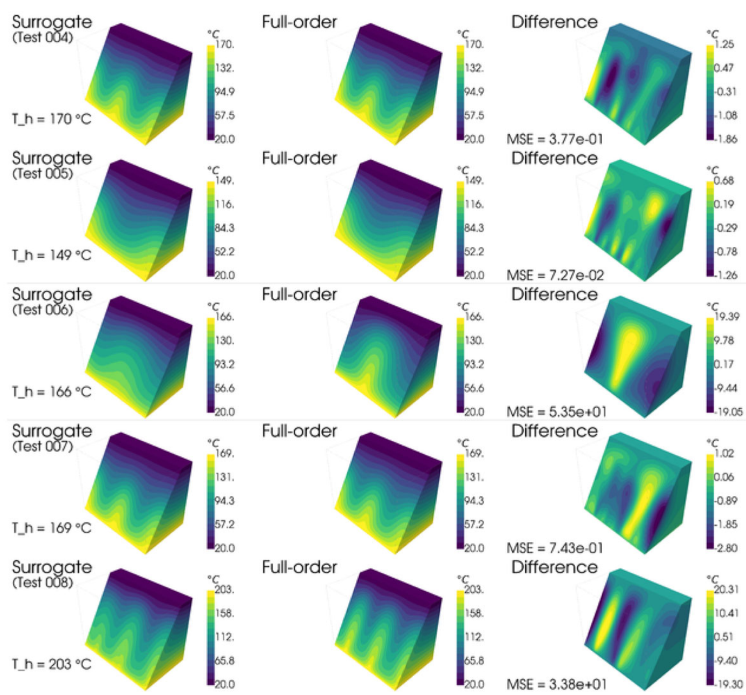

Fig. 17 Samples 04-08 from the test data set in Fig. 3. The columns display the surrogate's predicted temperature field (left), the full-order solution (middle), and the difference between the two (right)

Appendix B: Test data Fig. 4

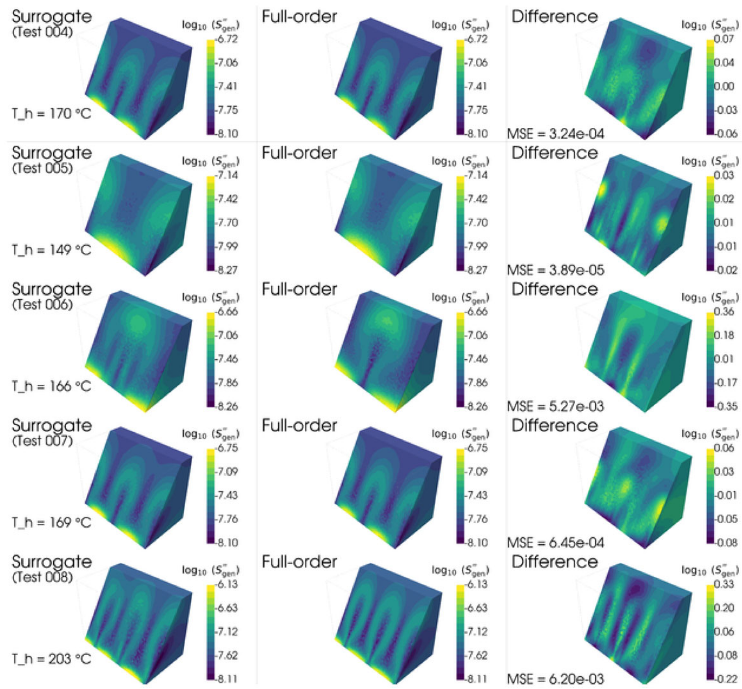

Fig. 18 Samples 04-08 from the test data set in Fig. 4. The columns display the surrogate's predicted entropy generation field (left), the full-order solution (middle), and the difference between the two (right)

Acknowledgements The authors greatly acknowledge the funding provided by the Ministry of Economic Affairs, Industry, Climate Action and Energy of the State of North Rhine-Westphalia and the European Union (grant KarboEx2 EFRE-20800290). Contributions by Denise Degen were made under the grant from the German Federal Ministry of Research, Technology and Space (grant PBML-HM 16|S24062). Furthermore, the COMSOL Multiphysics® simulations could be carried out via the Python API developed by Hennig et al. [91].

Author Contributions TS carried out the simulations and drafted the paper. DD supported the conceptualization, interpretation, and writing the manuscript. TM, HR, and FW were responsible for reviewing the concepts and reviewing and editing the manuscript. Furthermore, all authors read and approved the final paper.

Funding Open Access funding enabled and organized by Projekt DEAL. This research has been supported by the Ministry of Economic Affairs, Industry, Climate Action and Energy of the State of North Rhine-Westphalia and the European Union (grant no. EFRE-20800290), geomecon GmbH, HarbourDom GmbH, and the German Federal Ministry of Research, Technology and Space (grant no. 16|S24062).

Data Availability The training and validation data sets, their associated model parameters, and the NI-RB and neural network code for the construction of all surrogate models are published in the following Zenodo repository: https://doi.org/10.5281/zenodo.17473344.

Declarations

Competing interests The authors declare no competing interests.

References

1. Liu, C.H., Massarweh, O., Abushaikha, A.S.: Numerical simulation on geosystem Thermal-Hydro-Mechanical-Chemical coupling: A review. Geoenergy Sci. Eng. **254**, 214059 (2025). https://doi.org/10.1016/j.geoen.2025.214059
2. Kolditz, O., Shao, H., Wang, W., Nagel, T., Bauer, S. (eds.): Thermo-hydro-mechanical-chemical Processes in Fractured Porous Media: Modelling and Benchmarking: from Benchmarking to Tutoring. Terrestrial Environmental Sciences. Springer, Cham (2018). https://doi.org/10.1007/978-3-319-68225-9
3. Vallier, B., Magnenet, V., Schmittbuhl, J., Fond, C.: THM modeling of hydrothermal circulation at Rittershoffen geothermal site. France. Geotherm. Energy **6**(1), 22 (2018). https://doi.org/10.1186/s40517-018-0108-1
4. Degen, D., Caviedes Voullième, D., Buiter, S., Hendricks Franssen, H.-J., Vereecken, H., González-Nicolás, A., Wellmann, F.: Perspectives of physics-based machine learning strategies for geoscientific applications governed by partial differential equations. Geosci. Model Dev. **16**(24), 7375–7409 (2023). https://doi.org/10.5194/gmd-16-7375-2023
5. Patterson, J.W., Driesner, T.: Elastic and thermoelastic effects on thermal water convection in fracture zones. J. Geophys. Res. Solid Earth **126**(2), 2020–020940 (2021). https://doi.org/10.1029/2020JB020940
6. Bejan, A.: Convection heat transfer, 4th edn. Wiley, New Jersey (2013). https://doi.org/10.1002/9781118671627
7. Niederau, J., Börsing, N., Wellmann, F., Clauser, C.: Entropy production and attractors: Measures to quantify uncertainty and complexity introduced by convection. In: EGC 2016, Strasbourg, France (2016)
8. Park, J.: Uncertainty quantification and sensitivity analysis of geoscientific predictions with data-driven approaches. Dissertation, Stanford University, California (2019). https://purl.stanford.edu/qc240rr6278
9. Bauer, P., Dueben, P.D., Hoefler, T., Quintino, T., Schulthess, T.C., Wedi, N.P.: The digital revolution of Earth-system science. Nat. Comput. Sci. **1**(2), 104–113 (2021). https://doi.org/10.1038/s43588-021-00023-0
10. Degen, D., Veroy, K., Wellmann, F.: Uncertainty quantification for basin-scale geothermal conduction models. Sci. Rep. **12**(1), 4246 (2022). https://doi.org/10.1038/s41598-022-08017-2
11. Yan, B., Gudala, M., Sun, S.: Robust optimization of geothermal recovery based on a generalized thermal decline model and deep learning. Energy Convers. Manage. **286**, 117033 (2023). https://doi.org/10.1016/j.enconman.2023.117033
12. Parsa, S.M.: Physics-informed machine learning meets renewable energy systems: A review of advances, challenges, guidelines, and future outlooks. **402**, 126925. https://doi.org/10.1016/j.apenergy.2025.126925
13. Kruszewski, M., Verdecchia, A., Heidbach, O., Harrington, R., Healy, D.: Evolution of fault reactivation potential in deep geothermal systems. Insights from the greater Ruhr region, Germany (2023). https://doi.org/10.5194/egusphere-2023-1889
14. Agemar, T., Hese, F., Moeck, I., Stober, I.: Kriterienkatalog für die Erfassung tiefreichender Störungen und ihrer geothermischen Nutzbarkeit in Deutschland. Zeitschrift der Deutschen Gesellschaft für Geowissenschaften **168**(2), 285–300 (2017). https://doi.org/10.1127/zdgg/2017/0084
15. Frey, M., Van Der Vaart, J., Bär, K., Bossennec, C., Calcagno, P., Dezayes, C., Sass, I.: Techno-economic assessment of geothermal resources in the variscan basement of the Northern Upper Rhine Graben. Nat. Resour. Res. **32**(1), 213–234 (2023). https://doi.org/10.1007/s11053-022-10138-4
16. Rühaak, W., Rath, V., Clauser, C.: Detecting thermal anomalies within the Molasse Basin, southern Germany. Hydrogeol. J. **18**(8), 1897–1915 (2010). https://doi.org/10.1007/s10040-010-0676-z
17. Guillou-Frottier, L., Milesi, G., Roche, V., Duwiquet, H., Taillefer, A.: Heat flow, thermal anomalies, tectonic regimes and high-temperature geothermal systems in fault zones. Comptes Rendus. Géosci. **356**(S2), 389–421 (2024). https://doi.org/10.5802/crgeos.213
18. Duwiquet, H.: Crustal Fault Zones as geothermal power systems. Contribution of numerical modelling and comparison with natural systems. PhD thesis, Université d'Orléans (2022). https://theses.hal.science/tel-03591286v2
19. Ringrose, P., Bentley, M.: Reservoir model design: A practitioner's guide. Springer, Cham (2021). https://doi.org/10.1007/978-3-030-70163-5
20. Faulkner, D.R., Jackson, C.A.L., Lunn, R.J., Schlische, R.W., Shipton, Z.K., Wibberley, C.A.J., Withjack, M.O.: A review of recent developments concerning the structure, mechanics and fluid flow properties of fault zones. J. Struct. Geol. **32**(11), 1557–1575 (2010). https://doi.org/10.1016/j.jsg.2010.06.009
21. Cross, M.C., Hohenberg, P.C.: Pattern formation outside of equilibrium. Rev. Mod. Phys. **65**(3), 851–1112 (1993). https://doi.org/10.1103/RevModPhys.65.851
22. Taylor, R.L.V., David, J.: Attractors: Nonstrange to Chaotic. SIAM Undergrad. Res. Online **4**, 72–80 (2011). https://doi.org/10.1137/10S01079X
23. Guillou-Frottier, L., Duwiquet, H., Launay, G., Taillefer, A., Roche, V., Link, G.: On the morphology and amplitude of 2D and 3D thermal anomalies induced by buoyancy-driven flow within and around fault zones. Solid Earth **11**(4), 1571–1595 (2020). https://doi.org/10.5194/se-11-1571-2020

24. Magri, F., Möller, S., Inbar, N., Möller, P., Raggad, M., Rödiger, T., Rosenthal, E., Siebert, C.: 2D and 3D coexisting modes of thermal convection in fractured hydrothermal systems - Implications for transboundary flow in the Lower Yarmouk Gorge. Mar. Pet. Geol. **78**, 750–758 (2016). https://doi.org/10.1016/j.marpetgeo.2016.10.002
25. Magri, F., Cacace, M., Fischer, T., Kolditz, O., Wang, W., Watanabe, N.: Thermal convection of viscous fluids in a faulted system: 3D benchmark for numerical codes. Energy Proc. **125**, 310–317 (2017). https://doi.org/10.1016/j.egypro.2017.08.204
26. Khotyachuk, R., Johannsen, K.: Analysis of the numerical solutions of the elder problem using big data and machine learning. Big Data Cognit. Comput. **7**(1), 52 (2023). https://doi.org/10.3390/bdcc7010052
27. Hesthaven, J.S., Ubbiali, S.: Non-intrusive reduced order modeling of nonlinear problems using neural networks. J. Comput. Phys. **363**, 55–78 (2018). https://doi.org/10.1016/j.jcp.2018.02.037
28. Swischuk, R., Mainini, L., Peherstorfer, B., Willcox, K.: Projection-based model reduction: Formulations for physics-based machine learning. Comput. Fluids **179**, 704–717 (2019). https://doi.org/10.1016/j.compfluid.2018.07.021
29. Börsing, N., Wellmann, J.F., Niederau, J., Regenauer-Lieb, K.: Entropy production in a box: Analysis of instabilities in confined hydrothermal systems. Water Resour. Res. **53**(9), 7716–7739 (2017). https://doi.org/10.1002/2017WR020427
30. Niederau, J., Wellmann, J.F., Börsing, N.: Analyzing the influence of correlation length in permeability on convective systems in heterogeneous aquifers using entropy production. Geotherm. Energy **7**(1), 35 (2019). https://doi.org/10.1186/s40517-019-0151-6
31. Bundschuh, J.: Introduction to the numerical modeling of groundwater and geothermal systems: Fundamentals of mass, energy and solute transport in poroelastic rocks, 1st, ed Multiphysics Modeling Series. Taylor & Francis Group, Milton (2010)
32. Zyvoloski, G.A., Robinson, B.A., Dash, Z.V., Trease, L.L.: Summary of the models and methods for the FEHM application - a finite-element heat- and mass-transfer code. Technical Report LA–13307-MS, 565545, Los Alamos National Laboratory (1997). https://doi.org/10.2172/565545
33. Berre, I., Doster, F., Keilegavlen, E.: Flow in fractured porous media: A review of conceptual models and discretization approaches. **130**(1), 215–236 (2019). https://doi.org/10.1007/s11242-018-1171-6
34. Pola, M., Cacace, M., Fabbri, P., Piccinini, L., Zampieri, D., Torresan, F.: Fault control on a thermal anomaly: Conceptual and numerical modeling of a low-temperature geothermal system in the Southern Alps Foreland Basin (NE Italy). J. Geophys. Res. Solid Earth **125**(5), 2019–017394 (2020). https://doi.org/10.1029/2019JB017394
35. Poulet, T., Lesueur, M., Kelka, U.: Dynamic modelling of overprinted low-permeability fault cores and surrounding damage zones as lower dimensional interfaces for multiphysics simulations. Comput. Geosci. **150**, 104719 (2021). https://doi.org/10.1016/j.cageo.2021.104719
36. COMSOL AB: Subsurface Flow Module - User's Guide vol. 6.3. COMSOL Multiphysics®, Sweden (2024)
37. Nield, D.A.: Convection in porous media, 3rd, ed Springer, New York, NY (2006)
38. COMSOL AB: Heat transfer module user's guide vol. 6.3. COMSOL Multiphysics®, Sweden (2024)
39. Horton, C.W., Rogers, F.T.: Convection currents in a porous medium. J. Appl. Phys. **16**(6), 367–370 (1945). https://doi.org/10.1063/1.1707601
40. Lapwood, E.R.: Convection of a fluid in a porous medium. Math. Proc. Cambridge Philos. Soc. **44**(4), 508–521 (1948). https://doi.org/10.1017/S030500410002452X
41. Zhao, C., Hobbs, B.E., Ord, A.: Convective and advective heat transfer in geological systems. Advances in geophysical and environmental mechanics and mathematics. Springer, Berlin; London (2008)
42. Kevrekidis, I.G., Rico-Martínez, R., Ecke, R.E., Farber, R.M., Lapedes, A.S.: Global bifurcations in Rayleigh-Bénard convection. Experiments, empirical maps and numerical bifurcation analysis. Phys. D: Nonlinear Phenomena **71**(3), 342–362 (1994). https://doi.org/10.1016/0167-2789(94)90152-X
43. Pisarchik, A.N., Feudel, U.: Control of multistability. Phys. Rep. **540**(4), 167–218 (2014). https://doi.org/10.1016/j.physrep.2014.02.007
44. Oh, J.H., Kim, D.-G., Kim, D.H., Aodu, S.A., Park, I.S.: Influence of Prandtl number on the chaos transition for pure natural and Rayleigh-Bénard convections inside a rectangular cavity. Int. Commun. Heat Mass Transfer **155**, 107511 (2024). https://doi.org/10.1016/j.icheatmasstransfer.2024.107511
45. Beck, J.L.: Convection in a box of porous material saturated with fluid. Phys. Fluids **15**(8), 1377–1383 (1972). https://doi.org/10.1063/1.1694096
46. Huang, P.-W., Wellmann, F.: An explanation to the nusselt-rayleigh discrepancy in naturally convected porous media. Transp. Porous Media **137**(1), 195–214 (2021). https://doi.org/10.1007/s11242-021-01556-8
47. Nield, D.A.: Onset of thermohaline convection in a porous medium. Water Resour. Res. **4**(3), 553–560 (1968). https://doi.org/10.1029/WR004i003p00553
48. Lin, G., Zhao, C., Hobbs, B.E., Ord, A., Mühlhaus, H.B.: Theoretical and numerical analyses of convective instability in porous media with temperature-dependent viscosity. Commun. Numer. Methods Eng. **19**(10), 787–799 (2003). https://doi.org/10.1002/cnm.620
49. Murphy, H.D.: Convective instabilities in vertical fractures and faults. J. Geophys. Res. Solid Earth **84**(B11), 6121–6130 (1979). https://doi.org/10.1029/JB084iB11p06121

50. Malkovsky, V.I., Magri, F.: Thermal convection of temperature-dependent viscous fluids within three-dimensional faulted geothermal systems: Estimation from linear and numerical analyses. Water Resour. Res. **52**(4), 2855–2867 (2016). https://doi.org/10.1002/2015WR018001
51. Diersch, H.-J.G., Kolditz, O.: Variable-density flow and transport in porous media: approaches and challenges. Adv. Water Resour. **25**(8–12), 899–944 (2002). https://doi.org/10.1016/S0309-1708(02)00063-5
52. Bejan, A.: Entropy Generation Minimization: the Method of Thermodynamic Optimization of Finite-size Systems and Finite-time Processes. Advanced topicsc in mechanical engineering series. CRC Press, Boca Raton, Fla. (1996)
53. Bejan, A.: A study of entropy generation in fundamental convective heat transfer. J. Heat Transfer **101**(4), 718–725 (1979). https://doi.org/10.1115/1.3451063
54. Mahmud, S., Fraser, R.A.: The second law analysis in fundamental convective heat transfer problems. Int. J. Therm. Sci. **42**(2), 177–186 (2003). https://doi.org/10.1016/S1290-0729(02)00017-0
55. Magherbi, M., Abbassi, H., Ben Brahim, A.: Entropy generation at the onset of natural convection. Int. J. Heat Mass Transf. **46**(18), 3441–3450 (2003). https://doi.org/10.1016/S0017-9310(03)00133-9
56. Degen, D., Cacace, M., Wellmann, F.: 3D multi-physics uncertainty quantification using physics-based machine learning. Sci. Rep. **12**(1), 17491 (2022). https://doi.org/10.1038/s41598-022-21739-7
57. Loh, W.-L.: On Latin hypercube sampling. Ann. Stat. **24**(5) (1996). https://doi.org/10.1214/aos/1069362310
58. Paszke, A., Gross, S., Massa, F., Lerer, A., Bradbury, J., Chanan, G., Killeen, T., Lin, Z., Gimelshein, N., Antiga, L., Desmaison, A., Köpf, A., Yang, E., DeVito, Z., Raison, M., Tejani, A., Chilamkurthy, S., Steiner, B., Fang, L., Bai, J., Chintala, S.: PyTorch: An Imperative Style, High-Performance Deep Learning Library. arXiv (2019). https://doi.org/10.48550/ARXIV.1912.01703
59. Falcon, W.: The PyTorch lightning team: PyTorch lightning (2019). https://doi.org/10.5281/zenodo.3828935
60. Akiba, T., Sano, S., Yanase, T., Ohta, T., Koyama, M.: Optuna: a next-generation hyperparameter optimization framework. In: Proceedings of the 25th ACM SIGKDD International Conference on Knowledge Discovery and Data Mining (2019). https://doi.org/10.1145/3292500.3330701
61. Agemar, T., Schellschmidt, R., Schulz, R.: Subsurface temperature distribution in Germany. Geothermics **44**, 65–77 (2012). https://doi.org/10.1016/j.geothermics.2012.07.002
62. Scibek, J.: Multidisciplinary database of permeability of fault zones and surrounding protolith rocks at world-wide sites. Sci. Data **7**(1), 95 (2020). https://doi.org/10.1038/s41597-020-0435-5
63. Pederson, C., Mueller, M., Lippert, K., Igbokwe, O.A., Riechelmann, S., Lersch, S., Benger, P., Verdecchia, A., Immenhauser, A.: Impact of a regional fault zone on the properties of a deep geothermal carbonate reservoir unit (Devonian of NRW). Zeitschrift der Deutschen Gesellschaft für Geowissenschaften **172**(3), 339–364 (2021). https://doi.org/10.1127/zdgg/2021/0281
64. Bär, K., Reinsch, T., Bott, J.: P^3 - PetroPhysical property database. GFZ Data Serv. (2019). https://doi.org/10.5880/GFZ.4.8.2019.P3
65. Magri, F., Cacace, M., Fischer, T., Naumov, D., Wang, W., Watanabe, N., Zheng, T., Miao, X.-Y., Nagel, T., Walther, M.: HT (Convection) Processes. In: Kolditz, O., Nagel, T., Shao, H., Wang, W., Bauer, S. (eds.) Thermo-Hydro-Mechanical-Chemical Processes in Fractured Porous Media: Modelling and Benchmarking, pp. 157–177. Springer, Cham (2018). https://doi.org/10.1007/978-3-319-68225-9_7
66. Degen, D., Ziegler, M., Heidbach, O., Henk, A., Reiter, K., Wellmann, F.: About the trustworthiness of physics-based machine learning – a considerations for geomechanical applications. Tectonic plate interactions, magma genesis, and lithosphere deformation at all scales/Structural geology and tectonics, paleoseismology, rock physics, experimental deformation/Tectonics (2024). https://doi.org/10.5194/egusphere-2024-2932
67. Zhao, C., Hobbs, B.E., Ord, A., Peng, S., Mühlhaus, H.B., Liu, L.: Theoretical investigation of convective instability in inclined and fluid-saturated three-dimensional fault zones. Tectonophysics **387**(1–4), 47–64 (2004). https://doi.org/10.1016/j.tecto.2004.06.007
68. Elder, J.W., Simmons, C.T., Diersch, H.-J., Frolkovič, P., Holzbecher, E., Johannsen, K.: The elder problem. Fluids (2017). https://doi.org/10.3390/fluids2010011
69. Saltelli, A. (ed.): Global sensitivity analysis: The Primer. John Wiley, Chichester, England ; Hoboken, NJ (2008)
70. Degen, D., Wellmann, F.: Guidelines for sensitivity analyses in process simulations for solid earth geosciences. Appl. Math., (2024). https://doi.org/10.31223/X58H83
71. Saltelli, A.: Making best use of model evaluations to compute sensitivity indices. Comput. Phys. Commun. **145**(2), 280–297 (2002). https://doi.org/10.1016/S0010-4655(02)00280-1
72. Healy, D., Hicks, S.P.: De-risking the energy transition by quantifying the uncertainties in fault stability. Solid Earth. **13**(1), 15–39 (2022). https://doi.org/10.5194/se-13-15-2022
73. Guerrero-Martínez, F.J., Karimi, N., Ramos, E.: Numerical modeling of multiple steady-state convective modes in a tilted porous medium heated from below. Int. Commun. Heat Mass Transfer **92**, 64–72 (2018). https://doi.org/10.1016/j.icheatmasstransfer.2018.02.009
74. Xie, Y., Simmons, C.T., Werner, A.D., Diersch, H.G.: Prediction and uncertainty of free convection phenomena in porous media. Water Resour. Res. **48**(2), 2011–011346 (2012). https://doi.org/10.1029/2011WR011346

75. Horne, R.N., Caltagirone, J.-P.: On the evolution of thermal disturbances during natural convection in a porous medium. J. Fluid Mech. **100**(2), 385–395 (1980). https://doi.org/10.1017/S0022112080001218
76. Bodenschatz, E., Pesch, W., Ahlers, G.: Recent developments in Rayleigh-Bénard convection. Annu. Rev. Fluid Mech. **32**(1), 709–778 (2000). https://doi.org/10.1146/annurev.fluid.32.1.709
77. Guillou-Frottier, L., Carrė, C., Bourgine, B., Bouchot, V., Genter, A.: Structure of hydrothermal convection in the Upper Rhine Graben as inferred from corrected temperature data and basin-scale numerical models. J. Volcanol. Geoth. Res. **256**, 29–49 (2013). https://doi.org/10.1016/j.jvolgeores.2013.02.008
78. Magnenet, V., Fond, C., Genter, A., Schmittbuhl, J.: Two-dimensional THM modelling of the large scale natural hydrothermal circulation at Soultz-sous-Forêts. Geotherm. Energy **2**(1), 17 (2014). https://doi.org/10.1186/s40517-014-0017-x
79. Mezon, C., Mourzenko, V.V., Thovert, J.-F., Antoine, R., Fontaine, F., Finizola, A., Adler, P.M.: Thermal convection in three-dimensional fractured porous media. Phys. Rev. E **97**(1), 013106 (2018). https://doi.org/10.1103/PhysRevE.97.013106
80. Yan, G., Busch, B., Egert, R., Esmaeilpour, M., Stricker, K., Kohl, T.: Transport mechanisms of hydrothermal convection in faulted tight sandstones. Solid Earth **14**(3), 293–310 (2023). https://doi.org/10.5194/se-14-293-2023
81. Duwiquet, H., Magri, F., Lopez, S., Guillon, T., Arbaret, L., Bellanger, M., Guillou-Frottier, L.: Tectonic regime as a control factor for crustal fault zone (CFZ) Geothermal reservoir in an amagmatic system: A 3D dynamic numerical modeling approach. Nat. Resour. Res. **31**(6), 3155–3172 (2022). https://doi.org/10.1007/s11053-022-10116-w
82. Bächler, D., Kohl, T., Rybach, L.: Impact of graben-parallel faults on hydrothermal convection—-Rhine Graben case study. **28**(9–11), 431–441. https://doi.org/10.1016/S1474-7065(03)00063-9
83. Förster, A.: Analysis of borehole temperature data in the Northeast German Basin: continuous logs versus bottom-hole temperatures. Pet. Geosci. **7**(3), 241–254 (2001). https://doi.org/10.1144/petgeo.7.3.241
84. Santoso, R., Degen, D., Knapp, D., Pechnig, R., Wellmann, F.: Entropy production as a comprehensive indicator to address epistemic uncertainties - a case study of the Hague, Netherlands. In: 49th Workshop on Geothermal Reservoir Engineering, Stanford (2024)
85. Wellmann, J.F., Regenauer-Lieb, K.: Effect of geological data quality on uncertainties in geological models and subsurface flow fields. In: Thirty-Seventh Workshop on Geothermal Reservoir Engineering, vol. SGP-TR-194. Stanford University (2012)
86. Costa, V.A.F.: On natural convection in enclosures filled with fluid-saturated porous media including viscous dissipation. Int. J. Heat Mass Transf. **49**(13–14), 2215–2226 (2006). https://doi.org/10.1016/j.ijheatmasstransfer.2005.12.011
87. Adriano Cortes, Roberto Machado Velho, Gabriel Freguglia Barros, Fernando Alves Rochinha, Alvaro Luiz Gayoso De Azeredo Coutinho: Ablation study of a non-intrusive data-driven surrogate model for the Rayleigh-Bénard convection problem. Ibero-Latin American Congress on Computational Methods in Engineering (CILAMCE). (2024). https://doi.org/10.55592/cilamce.v6i06.10402
88. Willcox, K.E., Ghattas, O., Heimbach, P.: The imperative of physics-based modeling and inverse theory in computational science. Nat. Comput. Sci. **1**(3), 166–168 (2021). https://doi.org/10.1038/s43588-021-00040-z
89. Taillefer, A., Guillou-Frottier, L., Soliva, R., Magri, F., Lopez, S., Courrioux, G., Millot, R., Ladouche, B., Le Goff, E.: Topographic and faults control of hydrothermal circulation along dormant faults in an orogen. Geochem. Geophys. Geosyst. **19**(12), 4972–4995 (2018). https://doi.org/10.1029/2018GC007965
90. Simmons, C.T., Kuznetsov, A.V., Nield, D.A.: Effect of strong heterogeneity on the onset of convection in a porous medium: Importance of spatial dimensionality and geologic controls. Water Resour. Res. **46**(9), 2009–008606 (2010). https://doi.org/10.1029/2009WR008606
91. Hennig, J., Elfner, M., Maeder, A., Feder, J.: MPh-py/MPh: 1.2.4. Zenodo (2024). https://doi.org/10.5281/ZENODO.11539226

Authors and Affiliations

Thomas Simader[1,2,3] · Denise Degen[4,5] · Tobias Meier[1] · Horst Rüter[3] · Florian Wellmann[2,6]

✉ Thomas Simader
thomas.simader@geomecon.de

Denise Degen
degen@geo.tu-darmstadt.de

Tobias Meier
tobias.meier@geomecon.de

Horst Rüter
rueter@harbourdom.de

Florian Wellmann
florian.wellmann@cgre.rwth-aachen.de

1 geomecon GmbH, 10553 Berlin, Germany

2 Computational Geoscience, Geothermics and Reservoir Geophysics (CG3), RWTH Aachen University, 52062 Aachen, Germany

3 HarbourDom GmbH, 44287 Dortmund, Germany

4 Institute of Applied Geosciences, TU Darmstadt, 64287 Darmstadt, Germany

5 Section 4.5 Subsurface Process Modeling, GFZ Helmholtz Center for Geosciences, 14473 Potsdam, Germany

6 Fraunhofer Research Institution for Energy Infrastructures and Geothermal Systems IEG, 44801 Bochum, Germany